Numerical Investigation on the Salient Features of Flow over Standard Notchback Configurations using Scale Resolving Simulations

CHODE, K.K., VISWANATHAN, Harish and CHOW, K.

Numerical Investigation on the Salient Features of Flow over Standard Notchback Configurations using Scale Resolving Simulations

K. K. Chode [a], H. Viswanathan [a, b *], K. Chow [c]

[a] Materials and Engineering Research Institute, Sheffield Hallam University, Howard Street, Sheffield, England, S1 1WB, United Kingdom.

[b] Department of Engineering and Mathematics, Sheffield Hallam University, Howard Street, Sheffield, England, S1 1WB, United Kingdom

[c] HORIBA MIRA Ltd, Watling Street, Nuneaton Warwickshire, CV10 0TU, United Kingdom.

Highlights:

- SBES and SDES models agree reasonably well with experimental data for SAE T20 and SAE T40.
- SBES appears to resolve the flow structures marginally better than SDES.
- The transition from RANS to LES in SBES was found to be rapid and definitive in SSL.
- Flow features change significantly with a change in backlight angle.
- For SAE T30, the agreement between the model and experiment is less promising.

Keywords:

SAE Notchback Model; Non-symmetric flow; SBES; SDES; Vehicle Aerodynamics; Turbulence Modelling.

Abstract:

We present a detailed numerical investigation on the salient features of flow over an SAE reference body with several backlight angles representing a standard notchback geometry using Scale Resolving Simulations (SRS) such as the SBES and the SDES. A grid evaluation study is performed for the SAE Notchback geometry with 20° backlight angle

* Corresponding author. Email address: h.viswanathan@shu.ac.uk (H. Viswanathan); Phone: +0441142256244.

with a Reynolds number (*Re*) of 6.57 x 10^5 based on the height of the body. Various aerodynamic parameters and flow structures are compared against the previously published experimental results to evaluate the performance of the numerical predictions and against the unsteady $k - \omega$ SST model. Both SBES and SDES models agree well with the previously published wind tunnel results, exhibit a well-preserved modelled RANS layer, and numerically show minor differences between them. However, the transition from RANS to LES in the separated shear layer (SSL) appears to be marginally robust with SBES. Our numerical results demonstrate that with an increase in the backlight angle, the strength of trailing vortex tends to reduce on one side compensated by an increase on the other side of the model. As a consequence, the SSL shows a non-symmetrical flow feature behind the vehicle for the backlight angles of 30° and 40° as detailed in the experimental result and suitably predicted by the numerical results. We highlight that within the scope of this study, both the SRS models have shown to be accurate and reliable in predicting the aerodynamic force coefficients and flow features observed in experiments.

Nomenclature:

Re	Reynolds Number
U_∞	Freestream velocity
C_p	Coefficient of Pressure
k	Turbulence Kinetic Energy
ω	Specific Dissipation Rate
ν_t	Eddy/Turbulent Viscosity Ratio
S	Strain Rate magnitude
L_t	Turbulent Length Scale
θ	Backlight Angle
η_{nw}	Viscous boundary sublayer
l_{EI}	The inertial subrange
l_{DI}	The dissipative range
η	Kolmogorov length scale
λ_t	Taylor microscale
$\Delta x^+, \Delta y^+, \Delta z^+$	Dimensionless wall units
C_D	Drag Coefficient
C_L	Lift Coefficient
C_{Df}	Front Slant Drag Coefficient
C_{Dr}	Rear Slant Drag Coefficient
C_{Db}	Base Drag Coefficient
C_{Dp}	Pressure Drag Coefficient
e''	Center of Upper Recirculation bubble
e'	Center of Lower Recirculation bubble

Abbreviations:

RANS	Reynolds Averaged Navier Stokes
LES	Large Eddy Simulation
SRS	Scale Resolving Simulations
GIS	Grid Induced Separation
SDES	Shielded Detached Eddy Simulation

SBES	Stress Blended Eddy Simulation
RMS	Root Mean Square
SSL	Separated Shear Layer
TKE	Turbulence Kinetic Energy
TVR	Turbulent Viscosity Ratio

1. Introduction:

Numerical simulations of complex external flow physics present an area of significant interest during vehicle design and testing process, especially after the introduction of Worldwide harmonised Light vehicle Test Procedure (WLTP). The WLTP fundamentally changes homologation procedures for new vehicles, including a new test cycle that supersedes the previous New European Driving Cycle (NEDC) Cycle. The WLTP also imposes stringent regulations on vehicle manufacturers to limit emission and fuel consumption and requires a much larger number of vehicle details to be homologated, such as variations in wheel size. However, for the first time, WLTP allows the manufactures to evaluate fuel consumption measurements using numerical modelling techniques (Onishi et al., 2019), which increases the scope for virtual validation of vehicle designs. However, the numerical approaches used are required to model conditions much closer to reality, such as transient simulations, significantly increasing the complexity and requires High-Performance Computing (HPC) resources in the simulation of vehicle performance. Therefore, there is a need for further developing accurate and consistent turbulence modelling strategies that can be relied upon extensively in vehicle design and the development process.

1.1. Turbulence modelling Strategies:

The Reynolds Averaged Navier Stokes (RANS) turbulence approaches are obtained by temporally averaging the Navier-Stokes equations using Reynolds decomposition. In this approach, all range of turbulence scales is modelled using either two or more transport equations. Thus, RANS approaches are less complicated to model and have fewer computational resource requirements, but with the downside that any given space in the domain can only be represented by a single turbulence scale and not multiple scales as in reality. The commonly used RANS approaches are based on Eddy viscosity model, which are widely used in evaluating flow around bluff bodies. Most of the RANS approaches can predict large flow features accurately as shown by Ashton and Revell (2015), Ashton et al. (2016), Read and Viswanathan (2020) and Guilmineau et al. (2008, 2011) but for specific RANS approaches, the accuracy is shown to decrease when predicting the base pressure and aerodynamic characteristics such as drag and lift during situations where the adverse pressure gradients and separated flows are present when compared to experimental studies (Guilmineau, 2008; Han, 1989; Khalighi et al., 2001; Murakami, 1993; Rodi, 1997). LES methods are commonly adopted to overcome the aforementioned inaccuracies. However, the

use of LES methods is challenging as the filter width should ideally be the same as the smallest turbulent structure of interest, which results in very fine meshes near the walls. Additionally, the mesh should be sized to resolve the flow at least to 80% of TKE (Pope, 2000). This sizing of the mesh can lead to a significant increase in the overall cell count, substantially, increasing the computational resource requirements (Keogh et al., 2016; Krajnović and Davidson, 2005, 2002, 2001; Serre et al., 2013; Tsubokura et al., 2010, 2009).

Recent developments in turbulence modelling have led to multiple Scale Resolving Simulations (SRS) closures such as, but not restricted to Detached-Eddy Simulation (DES), Scale-Adaptive Simulation (SAS), and Wall Modelled LES (WMLES) etc. The hybrid RANS-LES methods rely on strong instability to generate turbulence structures in the separated zones (Menter et al., 2003; Shur et al., 2008; Spalart et al., 1997). SRS methods tend to provide a compromise between the accuracy and computational expense by switching over to subgrid-scale formulations in regions that require precise LES calculations, whereas, RANS calculations are carried out near solid boundaries or on regions of lower turbulence activity. Also, the DES methodology uses a filter based on the local grid resolution (cell length) to 'switch' between RANS and LES mode. Ideally, this 'switch' entrusts the whole boundary layer to a RANS model and the detached eddies to LES. A sudden switch to LES due to excessive refinement near walls results in a Grid Induced Separation (GIS) Menter and Kuntz (2004). Thus, to avoid the GIS, a shielding function is introduced into the transport equations to shield the RANS model from switching early to LES.

Modifications were introduced into the original DES model to incorporate the WMLES formulation and termed this model as Improved Delayed Detached Eddy Simulation(IDDES) (Gritskevich et al., 2013, 2012). However, this model may spuriously slow the transition from RANS to LES modes, and there was no clear distinction between RANS and LES regions and had to rely on a single subgrid model for LES mode. Therefore, it was essential to realise that the advanced DES formulations need a strong shielding function to fulfil the following requirements such as but not restricted to *i)* switch rapidly from RANS to LES in shear separation layers, *ii)* allow combinations of RANS with all algebraic subgrid-scale models of LES, and *iii)* remain robust even on mediocre quality meshes.

More recently, Menter (2018) developed two models, namely the Shielded Detached Eddy Simulation (SDES) and Stress Blended Eddy Simulation (SBES) based on the DES methodology. In the SDES formulation, a new shielding function and a new definition of the

grid-scale were proposed. SDES is expected to provide a rapid transition from RANS to LES mode and has an asymptotic shielding for RANS. Although SBES was developed based on the SDES, the RANS-LES blending is mathematically more robust; this is performed by introducing a shielding function based on the stress tensor and eddy-viscosity (Menter, 2018).

1.2. The Notchback Configurations:

The Ahmed body was first introduced by Ahmed et al. (1984) and has typically been the benchmark geometry for numerical and experimental validation studies (Aljure et al., 2014; Ashton et al., 2016; Ashton and Revell, 2015; Guilmineau, 2008; Guilmineau et al., 2011, 2018; Serre et al., 2013) owing to its simple design representing fundamental aerodynamic features of a vehicle such as rear windscreen "backlight" angle and vehicle base area resulting in similar flow features at the rear. However, the front-end design of Ahmed body deviates considerably from the actual vehicle as the design ignores features such as windshield and A-pillar, resulting in a smooth flow. Thus newer generic geometries representing realistic vehicle design configurations were proposed and analysed (Aljure et al., 2014; Cogotti, 1998; Heft et al., 2012).

Simplified vehicle geometries such as the SAE reference body (Cogotti, 1998) and the Windsor body (Le Good and Garry, 2004) are still evolving and are being used for time-accurate investigations, validation and calibration. These simplified vehicle geometries not only offer the advantage of a reasonable computational and experimental effort when compared to realistic vehicle test bodies such as DrivAer vehicle (Aljure et al., 2018; Ashton et al., 2016; Collin et al., 2016; Indinger and Adams, 2012) but also offer a broad spectrum of both numerical and experimental validation data. However, to date, there is little effort made to understand the flow structures over standard notchback configurations. Contemporary studies have nevertheless used in-house based LES codes on realistic notchback vehicles to understand the effect of shape configuration on pitching instability (Cheng et al., 2012, 2011).

Wood et al. (2014) have examined the standard SAE reference body with 20° backlight angle representing a notchback design as inherited from Cogotti (1998). Particle Image Velocimetry (PIV) technique was used to investigate the SAE reference body with 20° backlight angle on a 1:5 scale at Loughborough University's Wind Tunnel. The experimental results from Wood et al. (2014) showed flow structures that depict shear layer asymmetry with dominating trailing vortex on the right side of the body. The authors highlight that the

asymmetry present in the notchback flow is due to the difference in the strength of the trailing vortex. It is reported that the right-side vortex is ≈15% stronger than the left-hand side vortex. Wood (2015) observed that the increase in the backlight angle increases the separation due to worsening adverse pressure gradients, which further lead to the formation of the hairpin vortex on the backlight. Subsequently, Islam and Thornber (2017) studied the SAE notchback reference body with 20^0 backlight angle without diffuser and struts to validate their DES algorithm by incorporating a fully compressible solver. Their results over-predicted the coefficients of drag and lift by 14.5% and 21.3% respectively. The authors observed that the CFD results were uniform in spanwise velocity plots while streamwise velocity plots predicted a smaller recirculation region when compared to the experimental PIV data. A difference of 6.7% is observed in the vortex core position and 6% difference in time-averaged C_p profiles and Root Mean Square (RMS) values such as surface pressure and velocity fluctuations.

1.3. Motivation and Scope:

The newly developed SRS formulations such as the SBES and SDES have shown to be promising in overcoming problems such as *a)* The GIS due to mesh refinement on the RANS region affected by grid limiters, and *b)* Slow transition from RANS to LES at the Separating Shear Layer (SSL). However, to date, those models have only been employed for simple geometries such as a CS0 diffuser, flat plate and wind turbine blade recently (Menter, 2018, 2015; Rezaeiha et al., 2019). The outcomes from the studies mentioned above have shown that both SDES and SBES were able to predict the flow structures much better than other DES counterparts due to their strong shielding functions helping the formulation to switch rapidly from RANS to LES mode.

Our objective in the present work is at least two-fold; namely, *i)* to attempt a comparison between the SBES and SDES closures against the widely used URANS model on a standard notchback geometry where SSL has shown to be dominant experimentally. *ii)* to evaluate the accuracy of the aforementioned turbulence closures by varying the backlight angle configurations to examine the salient features of a notchback vehicle. At every stage, we shall validate our numerical predictions by comparing the experimental results of Wood et al. (2014) and Wood (2015).

2. Turbulence models

In the present study, three different turbulence models are assessed using the SAE reference body used by Wood et al. (2014), namely: $k-\omega$ SST, SDES and SBES.

2.1. $k-\omega$ SST (URANS):

The transport equation of k and ω in $k-\omega$ SST (Shear Stress Transport) are given by Equ.1 and 2. This model uses the $k-\omega$ formulation in the inner parts of the boundary layer and away from the wall, it behaves like $k-\varepsilon$ model for dealing with turbulent flows.

$$\frac{\partial \rho k}{\partial t}+\frac{\partial}{\partial x_i}(\rho u_i k)=P_k-\rho c_\mu k\omega+\frac{\partial}{\partial x_i}\left[\left(\mu+\frac{\mu_t}{\sigma_k}\right)\frac{\partial k}{\partial x_j}\right] \tag{1}$$

$$\frac{\partial \rho \omega}{\partial t}+\frac{\partial}{\partial x_i}(\rho u_i \omega) = \alpha\frac{\omega}{k}P_k-\rho\beta\omega^2+\frac{\partial}{\partial x_i}\left[\left(\mu+\frac{\mu_t}{\sigma_\omega}\right)\frac{\partial \omega}{\partial x_j}\right] + 2(1-F_1)\frac{\rho}{\omega,2}\frac{1}{\omega}\frac{\partial k}{\partial x_j}\frac{\partial \omega}{\partial x_j} \tag{2}$$

The constant parameter in production term and diffusion term of ω, φ (α, β) is defined as

$$\varphi = F_1\,\varphi_1+(1-F_1)\,\varphi_2 \tag{3}$$

Where F_1 is the blending function and is defined as Equ.4.

$$F_1=tanh\left\{\left\{min\left[\left(max\left(\frac{\sqrt{k}}{\beta^*\omega d},\frac{500\mu}{d^2\rho\omega}\right),\frac{4\rho\sigma_{\omega 2}k}{CD_{k\omega}d^2}\right)\right]\right\}^4\right\} \tag{4}$$

Where $CD_{k\omega}=max\left[\left(2\rho\sigma_{\omega,2}(1/\omega)(\partial k/\partial x_i)\,(\partial\omega/\partial x_i)\right),10^{-10}\right]$ and d is the distance from the nearest solid surface. The model constants are β^* = 0.09, α_1 = 0.5556, α_2 = 0.44, β_1 = 0.075, and β_2 = 0.0828.

The pitfall of the standard $k-\omega$ and $k-\varepsilon$ models is that they may lead to over-prediction of eddy-viscosity. Therefore, a new limiter was introduced in the formulation of eddy-viscosity to overcome this, given by Equ.5.

$$v_t=\frac{\alpha_1\rho k}{\max(\alpha_1\omega,SF_2)} \tag{5}$$

Where S is the scalar invariant of the strain rate (S_{ij}), $S=\sqrt{2S_{ij}S_{ij}}$, and F_2 is a second blending function defined as

$$F_2 = tanh\left\{\left[max\left(\frac{2\sqrt{k}}{\beta^*\omega d}, \frac{500\mu}{d^2\rho\omega}\right)\right]^2\right\} \quad (6)$$

Where α_1 = 0.31, k, and ω are the turbulent kinetic energy and the specific dissipation rate respectively.

2.2. Shielded Detached Eddy Simulation (SDES):

SDES is based on Delayed-DES (DDES) formulation, with an alternate shielding function as shown in Equ. 7. An additional sink term is added to the k equation to provide a strong shielding when shifting to LES mode. The shielding of this model is achieved by a new definition of mesh length scale in SDES is shown in Equ. 8.

$$F_{SDES} = \left[max\left(\frac{L_t}{C_{SDES}\Delta_{SDES}}(1 - f_s), 1\right) - 1\right] \quad (7)$$

$$\Delta_{SDES} = max\left[\sqrt[3]{vol}, 0.2\Delta_{max}\right] \quad (8)$$

The switch is activated when the eddy viscosity is reduced to the level comparable to the LES model. This reduction in eddy viscosity is achieved by equating the source and sink terms in k and ω in RANS equations, which results in an eddy viscosity equivalent to Equ. 9 which resembles the eddy viscosity definition of an SGS model.

$$v_t = \left[\left(\frac{\beta}{\alpha}\right)^{3/4} C_{SDES}\Delta\right]^2 S \quad (9)$$

The SDES constant (C_{SDES}) is calibrated in our model settings so that the product of $(\beta/\alpha)^{3/4}$ and C_{SDES} becomes 0.11, which is equal to Smagorinsky constant (C_s). The combination of $C_{SDES}\Delta$ enters the Smagorinsky formulation quadratically, thus resulting in a higher reduction in eddy viscosity levels when compared to the previous formulated version of DES (Menter, 2015).

2.3. Stress-Blended Eddy Simulation (SBES):

SBES is a re-evaluation of SDES formulation where an additional shielding function is introduced (Menter, 2018, 2015). This approach relies on the subtle formulation of the shielding function f_s to shield the boundary layer in RANS while quickly shifting to LES where applicable. The proposed shielding function is at the stress and eddy viscosity level given by τ_{ij} and v_t in Equ.10 and 11.

$$\tau_{ij}^{SBES} = f_s.\tau_{ij}^{RANS} + (1 - f_s)\tau_{ij}^{LES} \quad (10)$$

$$v_t^{SBES} = f_s.v_t^{RANS} + (1 - f_s).v_t^{LES} \quad (11)$$

The eddy viscosity and stress tensor switches to LES mode when f_s is zero, whereas if f_s is equal to one, then both the eddy viscosity and stress tensor will be in RANS mode.

3. Computational Approach and System Details:

3.1. Model Description and Computational Domain:

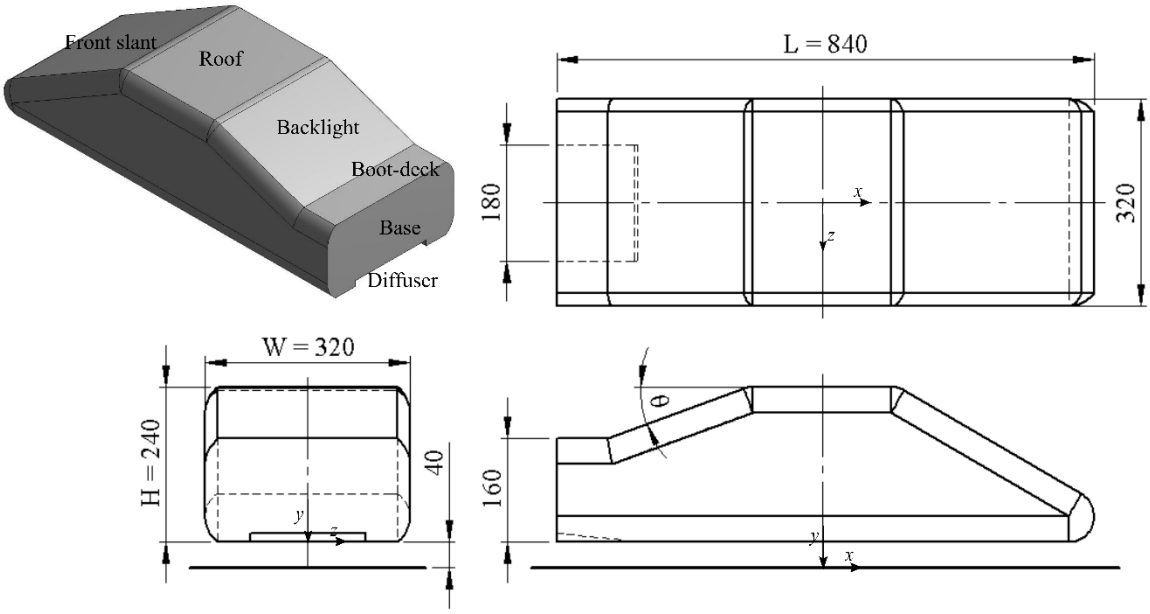

Fig. 1. The dimensions of the SAE notchback geometry are in mm and the backlight angle θ in degrees.

The geometry analysed in the present study is a 1:5 scale SAE reference body with 20°, 30°, and 40° backlight angles (θ) representing a notchback configuration that was experimentally investigated by Wood (2015) is shown in Fig. 1. In the experimental study of Wood (2015), the reference bodies were mounted on four cylindrical struts, at the height of y/H = -0.166 above the ground that contributes to 15.38% of the projected frontal area of the geometry shown in Fig. 1. The struts were neglected in the present study to avoid additional mesh complexity and are assumed to be negligible in their contribution, which is in line with the previously published literature on the Ahmed Body (Aljure et al., 2014; Ashton and Revell, 2015; Guilmineau, 2008). Thus, the geometry analysed are located at the same height of y/H = -0.166, above the floor. The SAE reference body with 20° backlight angle (SAE T20) is used for validating the simulations against an experimental investigation by Wood et al. (2014).

The computational domain Ω = 38.5H x 7H x 7H, shown in Fig. 2. is defined based on the ERCOFTAC guidelines adopted by several established research groups (Aljure et al., 2018, 2014; Ashton et al., 2016; Ashton and Revell, 2015; Evstafyeva et al., 2017; Guilmineau et al., 2018). The blockage ratio with the domain cross-section is 2.7%; whereas the experimental blockage ratio that was reported is 2.9%. Both the solid blockage and wake blockage corrections as per Mercker's Blockage Correction (Carr and Stapleford, 1986;

Mercker, 1986) are applied for aerodynamic coefficients reported in the present computational effort for the sake of consistency with the experimentally reported values by Wood (2015) and Wood et al. (2014). For further details on Mercker's Blockage corrections, the readers are directed to pp:47-49 in Wood (2015).

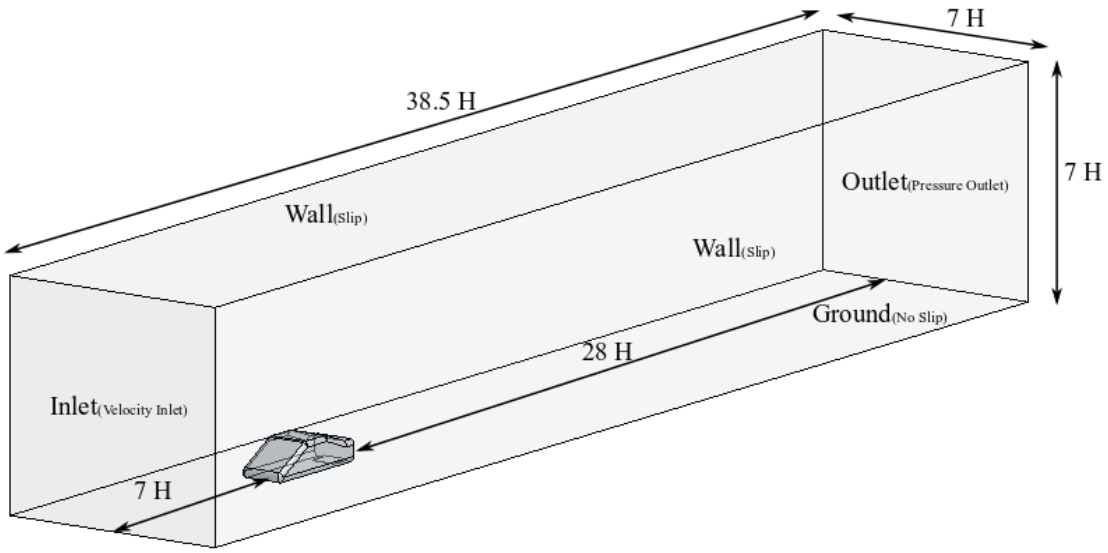

Fig. 2. Layout of the computational domain with normalised dimensions and the specified boundary conditions.

3.2. Length Scale Estimations and Grid Generation:

For the SAE T20 configuration, the length scale estimates are based on estimates made by Howard and Pourquie (2002) for an Ahmed body which are later used by Fares (2006) and Guilmineau et al. (2018). The boundary layer thickness around the vehicle can be determined by using Reynolds Number, $Re_H = u_\infty H/\nu$ based on H of the body, as shown in Fig. 1. The flow-dependent length scales such as the turbulent boundary layer thickness is estimated using $\delta/H \approx 0.37 Re_H^{-0.2}$, and the viscous boundary sublayer is estimated using $\eta_{nw}/L \approx 5.9\ Re_H^{-0.9}$. The largest energy-containing anisotropic structures (l_o) can be estimated by $l_o \approx \eta Re_H^{3/4}$, whereas, the inertial subrange, l_{EI} and dissipative range, l_{DI} can be estimated by $l_{EI} = l_o/6$ and $l_{DI} = 60\eta$. The Taylor microscale associated with the integral motion in the wake and Kolmogorov length scale associated with the smallest turbulent scale of the wake is estimated similar to that presented by Guilmineau et al. (2018), $\lambda_t \approx 4.6 Re_H^{-0.5}$ and $\eta \approx 0.998 Re_H^{-0.75}$ respectively. As a rationality check, a comparison of the estimated length scale for the SAE T20 configuration and the Ahmed body is summarised in Table 1.

Table 1

Comparison of the estimated characteristic length scales of the Ahmed body (Guilmineau et al., 2018) and SAE T20 (Present Study).

	η	λ_t	l_0	l_{EI}	l_{DI}	η_{nw}
Ahmed Body (Guilmineau et al., 2018)						
in mm	0.013	1.8074	345.6	57.6	0.799	0.0098
SAE T20 – Present Study						
in mm	0.012	1.6282	266	48	0.776	0.0093

The meshes used in the present study are generated using the Cut-Cell methodology that consists of unstructured hexahedral elements. The mesh sizes are determined by using two approaches *a)* normalised wall units and *b)* length scales estimations. The recommended normalised wall units for LES by Piomelli and Chasnov (1996) are $\Delta x^+ = 50 - 150$, $\Delta y^+ < 1$ and $\Delta z^+ = 15 - 40$. Where Δx^+, Δy^+ and Δz^+ are normalised wall units in x, y and z directions respectively. Normalised wall units are defined as shown in Equ.15.

$$\Delta x^+ = (u_t)_x / \nu, \Delta y^+ = (u_t)_y / \nu, \Delta z^+ = (u_t)_z / \nu \quad (15)$$

Where, $(u_t)_x$, $(u_t)_y$, $(u_t)_z$ correspond to the friction velocities in all three directions, and ν is the viscosity of the fluid.

The cell size on the surface of the body is determined to ensure the normalised wall units are within the recommended ranges. In the Cut-Cell method, a book type (rectangular cuboid) cell is generated in which the Δx and Δz are approximately the same (Shur et al., 2008), and Δy is much less than the other two dimensions. The summary of the normalised wall units used in the present study for all the grids is detailed in Table 2.

Table 2

Comparison of mesh resolution assessment range for SAE T20 (Present Study) and the Ahmed body (Ashton and Revell, 2015).

	Δx^+	Δy^+	Δz^+	Δ/η	**Cell Count**
WRLES Recommendation (Fröhlich et al., 2005; Piomelli and Chasnov, 1996)	50 – 150	< 2	15 – 40	<12	–
Ahmed Body (Fine Case) (Ashton and Revell, 2015)	10 – 150	0.1 – 0.5	5 – 70	40 – 110	16 x 10^6
Grid 1(present work)	200 – 380	0.9	200 – 380	240 – 650	2.91 x10^6
Grid 2 (present work)	100 – 250	0.9	100 – 250	80 – 320	8.57 x10^6
Grid 3 (present work) (on the backlight) (includes TB on the backlight)	100 – 250 100 – 150	0.9	100 – 250 100 – 150	64 – 320	14.55 x 10^6
Grid 4 (present work) (on the backlight) (includes TB on the backlight and DRs in the wake)	100 – 250 100 – 150	0.9	100 – 250 100 – 150	58 – 280	18.56 x10^6

For Grid 4, the flow domain is divided into four sub-domains from the centre of the model, as illustrated in Fig. 3. The height of the Focus Region (FR) is determined through analysing the wall shear effects, and the length of FR to adequately capture the near wake effects behind the vehicle. A refinement box called a Taylor Box (TB) is added around the backlight angle of the body, in which the cell sizes are equal to the Taylor microscale (λ_t) in line with Guilmineau et al. (2018). Further, refinement boxes called Domain Refinement (DR) are added to ensure a smooth transition. According to Fröhlich et al. (2005), a Δ/η value for Wall Resolved LES (WRLES) simulation should be < 12 in the freestream to ensure that a suitable amount of eddy dissipation resolved. For the current case, the Δ/η reported is as high as 240 near the backlight on the midplane at point (x = 140 mm, y = -208 mm) and Δ/η = 320 at (x = 580 mm, y = -190 mm) behind the model on the midplane for Grid 1 and for Grid

4 the values of Δ/η reported are 58 near the backlight and 120 behind the model. Grid 4 developed in this study is in line with values reported by Ashton and Revell (2015) and Guilmineau et al. (2018) for hybrid RANS-LES methods.

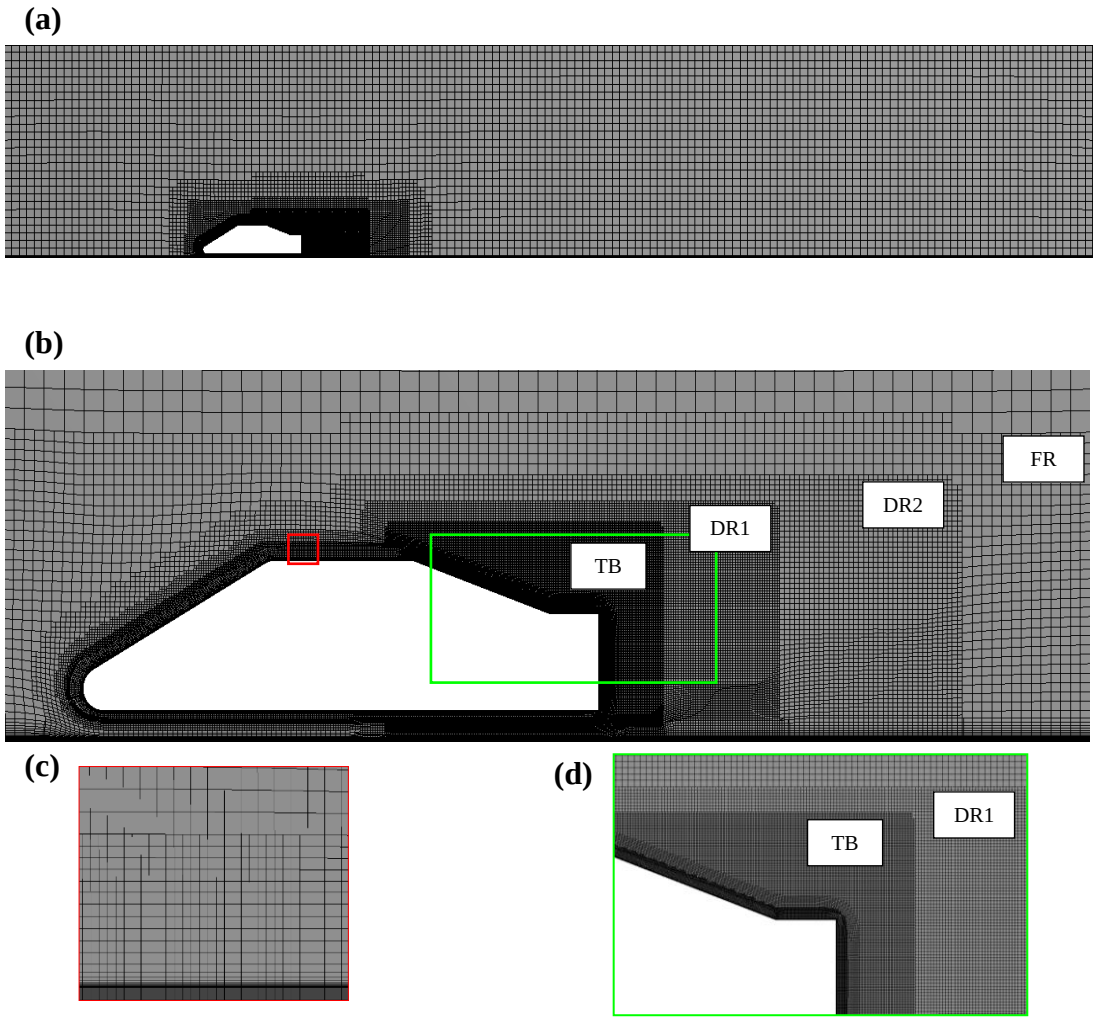

Fig. 3. Grid used in assessing turbulence models **a)** Cut in the xz-plane showing the grid distribution around the body. **b)** Detailed view of the mesh with highlighted zones *TB* – Taylor Box, *DR 1,2* – Domain Refinement, and *FR* – Focus Region. **c)** Detailed view of the boundary layer **d)** Detailed view of refinements behind the model.

3.3. Boundary Conditions:

The flow is at a Reynolds number of Re_H = 6.57 x 10^5 based on the height of the body H and the freestream velocity of (U_∞, 0, 0); where U_∞= 40 ms^{-1}. The turbulence intensity in the wind tunnel experiment reported by Wood et al. (2014) and Wood (2015) is approximately 0.2% that is specified at the inlet boundary. The flow was ensured to be fully developed with the boundary layer thickness of 60 mm before reaching the body as the inlet is placed x = 7H upstream of the vehicle. A zero-static pressure condition was applied to the outlet boundary located at x = 28H downstream of the vehicle. A no-slip wall condition is

imposed on the ground floor and body whereas slip condition is imposed on the remaining walls of the domain.

3.4. Solution Procedure and Computational Details:

The turbulence models were numerically solved using ANSYS Fluent Version 18.1. The present analysis is incompressible, and due to the turbulent nature of the wake, a pressure-based transient solver with a SIMPLE scheme for pressure-velocity coupling was used for all the simulations. For spatial discretisation, Bounded Central Differencing (BCD) was used to discretise the momentum equation. The BCD scheme is essentially a second-order central scheme, but it blends both second-order and first-order upwind schemes, the latter activating when the Convection Boundedness Criteria (CBC) is violated. A Third-order MUSCL scheme was used for discretising the Turbulent Kinetic Energy (TKE) and Specific Dissipation Rate (SDR). The pressure was discretised using second-order, whereas the Bounded second-order implicit formulation was applied for time discretisation. The flow field was initialised with the solution obtained through a steady-state RANS simulation based on the $k - \omega$ SST model. For SBES and SDES cases, the time step size of 2×10^{-5}s to ensure that the Courant-Friedrichs-Lewy (CFL) number < 1 in most of the regions. However, for the URANS case, a time step size of 2×10^{-4}s was used. The simulations were performed for over 30 convective cycles ($30 \times L/U_\infty$) for all the cases, and the unsteady statistics were obtained by averaging the flow for over last 20 convective flow units after it is first checked to have reached an asymptotic state.

The computational time for each simulation depends on the number of timesteps solved to achieve a statistically stationary flow and additionally for averaging the converged statistics for a sufficiently long time period. For instance, for Grid 4, which contained 18.56×10^6 elements, the total number of timesteps required are 3.1×10^4 to reach 30 convective cycles as mentioned above. The time taken per iteration is approximately equal to 1.6s on the Sheffield Hallam University (SHU) cluster with 128 CPUs. The total simulation time for completion is approximately 12 days. The computational time taken by all the turbulence models investigated is tabulated in Table 3.

Table 3

The computational expense for URANS and SRS simulations for SAE Reference body

Method	Temporal Scheme	Time Step (s)	No. of Cores	Wall time per iteration (s)	Total Compute Time
SST URANS	Transient	2×10^{-4}	128	1.2	131h (5 days)
SDES	Transient	2×10^{-5}	128	1.65	280h (12 days)
SBES	Transient	2×10^{-5}	128	1.65	280h (12 days)

4. Results and Discussion:

The results from this study are represented in three different sections to achieve systematic comparison between the *i)* experiment and turbulence models and *ii)* flow features arising from different backlight angle configurations. A grid-evaluation study is presented in **Section 4.1** to identify the mesh required. **Section 4.2** presents the comparison amongst the various turbulence models used in the present study and against the experimental data obtained by Wood (2015) and Wood et al. (2014) **Section 4.3** presents the influence of the backlight angle on aerodynamic force coefficients and flow structures and subsequently compared against the available experimental data (Wood, 2015).

4.1. Grid Evaluation:

The grid evaluation study was conducted using the SBES turbulence model. The grid was generated based on the procedure explained in **Section 3.2**. It is evident from Table 4 that summarises the aerodynamic force coefficients for all the grids, that both drag and lift coefficients are converged with Grid 4, while further mesh refinement may not result in a significant modification in the values predicted.

Table 4

Aerodynamic force coefficients assessed from the grid resolution study

Solver		Drag Coefficient (C_D)	Lift Coefficient (C_L)
SBES	Grid 1	0.1868	-0.1202
	Grid 2	0.1889	-0.1226
	Grid 3	0.1887	-0.1259
	Grid 4	0.1883	-0.1272

The time-averaged streamwise velocity plots (Fig. 4) indicate that all the grids predict the flow separation on the backlight angle; however, the wake behind the body shows moderate differences. Both Grid 3 and Grid 4 predicted a shear layer from the backlight which grows into the wake, and is strongly evidenced with Grid 4 and depletes at x = 620 mm.

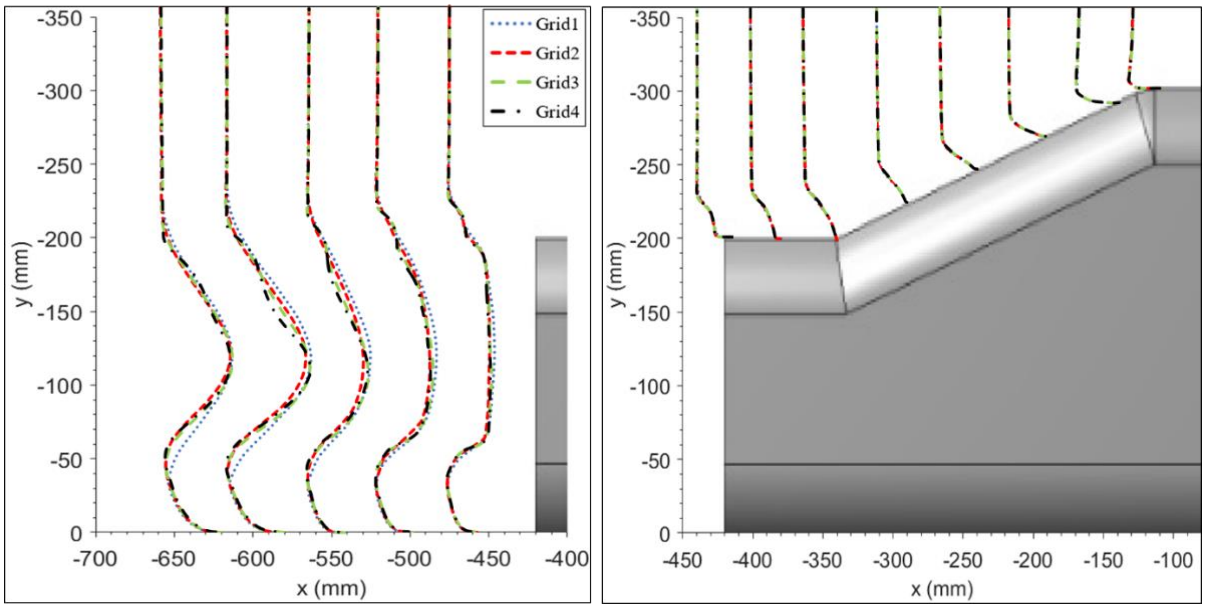

Fig. 4. Time-averaged Streamwise velocity profiles (right) over the backlight and in the wake (left) of SAE T20 body for various levels of grid refinement.

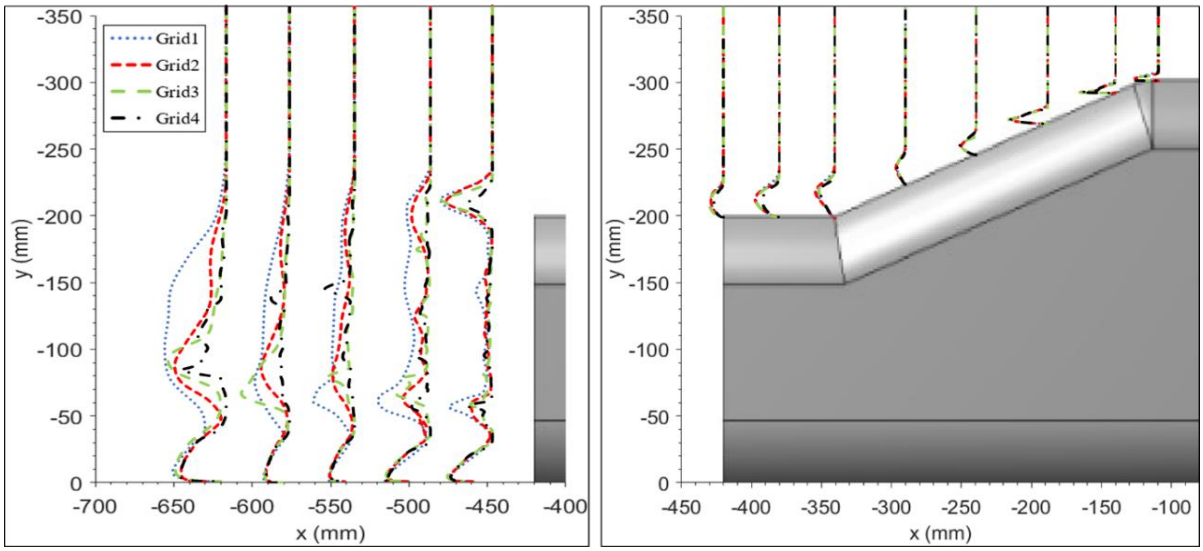

Fig. 5. Turbulent Kinetic Energy (*TKE*) profiles (right) over the backlight and in the wake (left) of SAE T20 body for various levels of grid refinement.

The TKE profile (Fig. 5) on the backlight show negligible differences between the grids analysed till x = 340 mm. However, after x = 340 mm Grid 4 shows a lower TKE indicating a better flow resolution on the boot-deck. In the wake of the body, Grid 1 tends to predict

higher TKE, and the size of the recirculation region suggests that there is less turbulent mixing, resulting in low resolution of the flow field as seen in Fig. 6. The lower TKE predicted by Grid 4 in the near wake region indicates that the flow is well resolved, which is a result of an additional DR region in the wake when compared to Grid 3. At this juncture, it is essential to highlight that, the Turbulent Viscosity Ratio (TVR), ν_t/ν, for a WRLES should be less than 10 (Fröhlich and von Terzi, 2008). However, for the current simulation the average value at location ($640< x <840$ mm, $0 < y < -180$ mm, $-0.1< z < 0.1$ mm) in the near wake, Grid 4 reported a value ≈ 42, whereas, for Grid 3, the value ≈ 98. Therefore, the Grid 4 is chosen to be appropriate for assessing the turbulence models and evaluate the salient features of the flow over the SAE reference bodies.

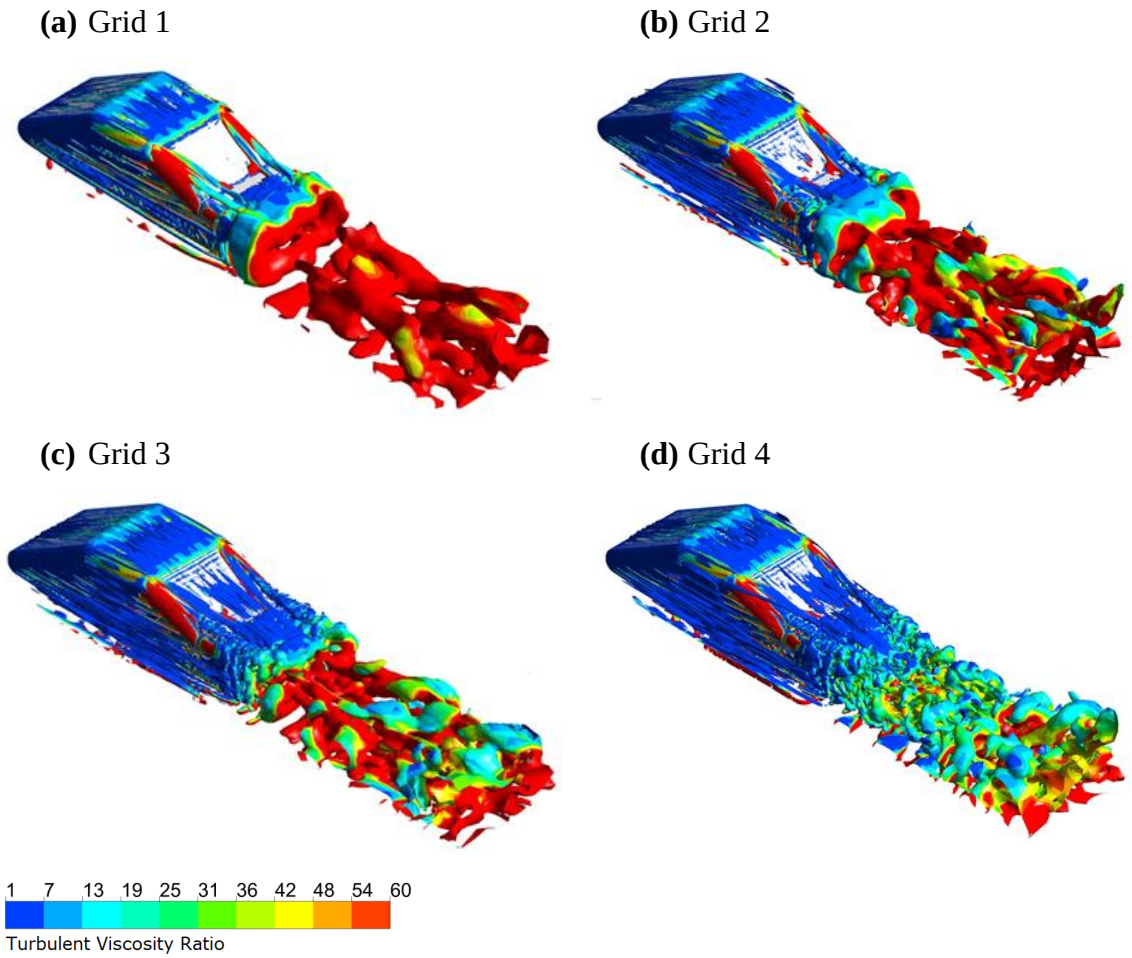

Fig. 6. Iso-surfaces of instantaneous Q-Criterion (0.014 s^{-2}) coloured by Turbulent Viscosity Ratio for various grids used in the present study.

4.2. Verification of Flow Features and Validation with Experimental Results:

4.2.1. Assessment of Flow Resolution:

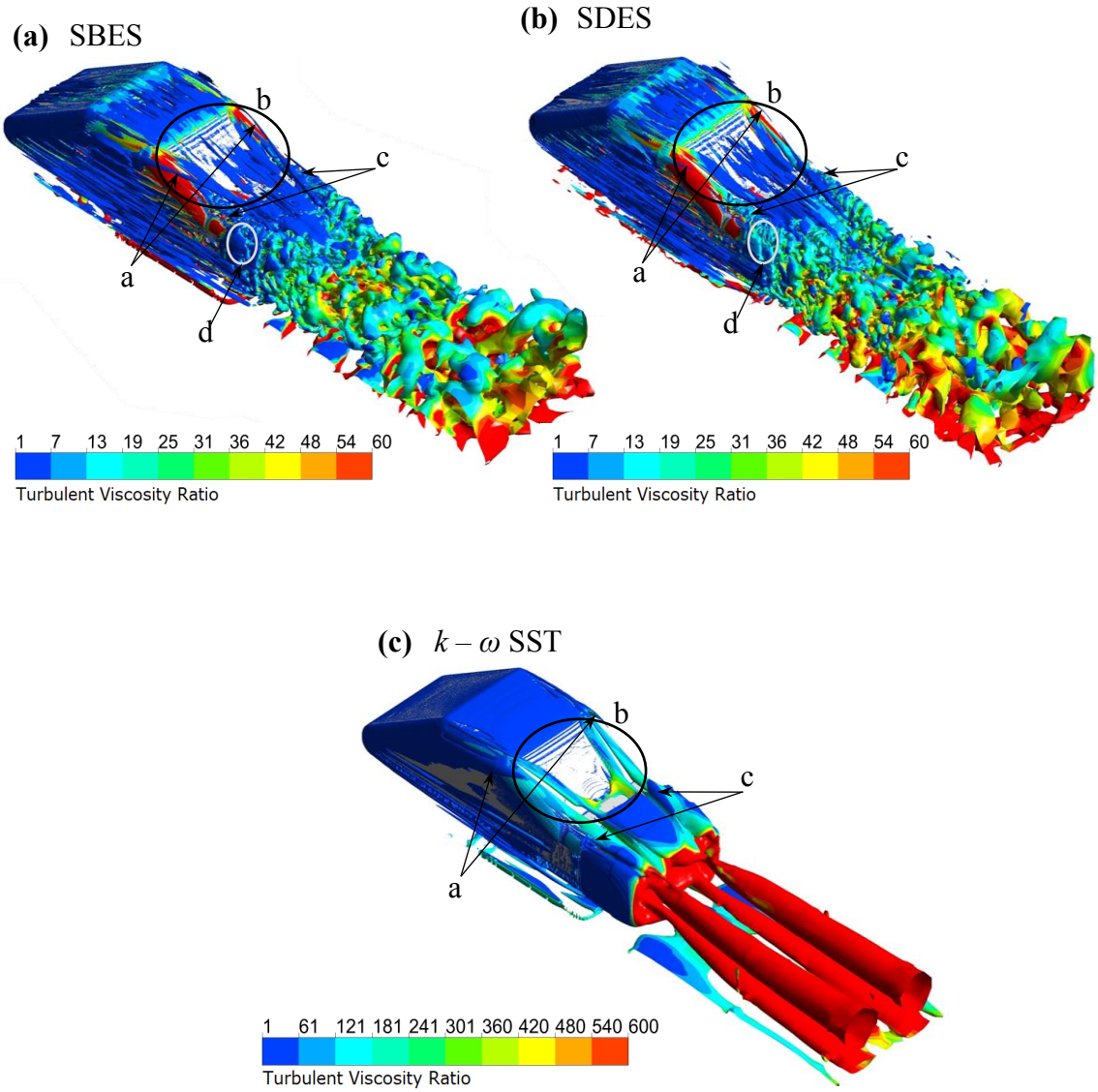

Fig. 7. Iso-surface of the instantaneous Q-criterion generated at 0.014 s^{-2} for all turbulence models and coloured by Turbulent Viscosity Ratio.

All the turbulence models predict the generic flow features of a typical notchback configuration, such as A-pillar vortex (*a*), flow separation over the backlight (*b*), and C-pillar vortex (*c*) as seen in Fig. 7. Qualitatively, no appreciable difference between flow structures predicted by SBES and SDES is evident except for the prediction of A-pillar vortex. Both SBES and SDES predict the internal flow features of the flow separation on the backlight much better than the $k-\omega$ SST model. However, quantitatively the near wake resolution in SBES appears to be better than that predicted by SDES. At the location highlighted (*d*) in Fig. 7, the average TVR predicted by SBES and SDES is approximately 7 and 13, respectively,

indicating that the resolution is better in SBES. This is further highlighted in the turbulence spectrum in the near wake shown by Fig. 8. At the outset, it can be observed that the energy cascade in the inertial subrange identified as the region between l_{EI} and l_{DI} predicted by both SBES and SDES is in good agreement with the theoretical slope of -5/3 (Pope, 2000). After approaching the l_{DI} which exists beyond the Taylor microscale (λ_t), exponential decay in energy indicates that the viscous effects are dominant in the dissipation range. In the dissipation range, although the prediction of cut-off wavenumber is the same, the SBES model tends to resolve eddies with higher energy than SDES.

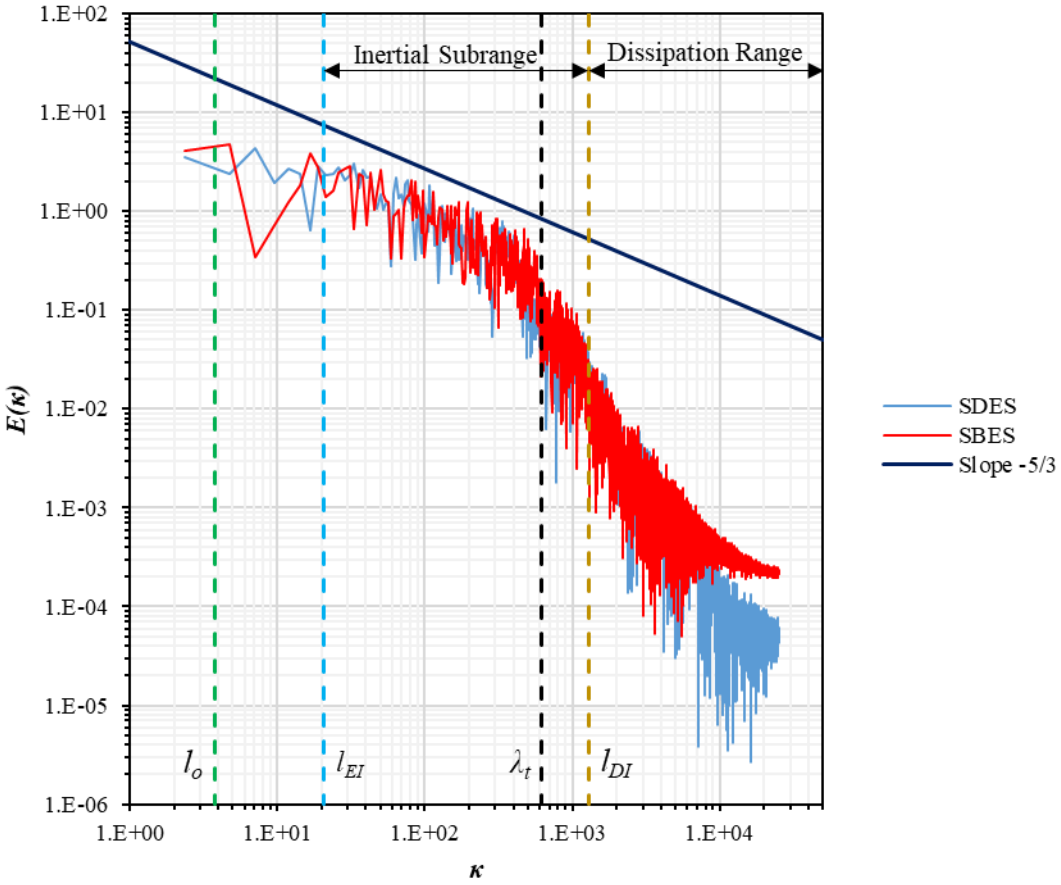

Fig. 8. The turbulence energy spectrum ($E(k)$) of SDES and SBES in the near wake of the model at point (x = 440 mm, y = -180 mm, z = 0).

A further assessment is carried out by examining the shielding of RANS boundary layer and levels of TVRs. Figs. 9(a) and (c) indicate the switch from RANS to LES for both SBES and SDES at the backlight and boot-deck respectively. The RANS mode is activated closer to the wall as indicated by F_{SDES} or F_{SBES} attaining 1, and LES mode is activated away from the wall as indicated by F_{SDES} or F_{SBES} reaching 0. Both SBES and SDES exhibit a well-preserved modelled RANS layer; however, the transition to LES that takes place in the SSL appears to be comparatively rapid and sharp with SBES, slightly improved compared to

SDES. This may be attributed to the improved asymptotic shielding formulation that blends the Reynolds Stresses between the RANS-LES regions discussed in **Section 2.3**. The corresponding eddy viscosity ratios shown by Figs. 9(b) and (d) indicate that the SBES produces lower eddy viscosity level at the SSL than the SDES and as a consequence, the shielding behaviour in SBES appears more refined to the flow topology.

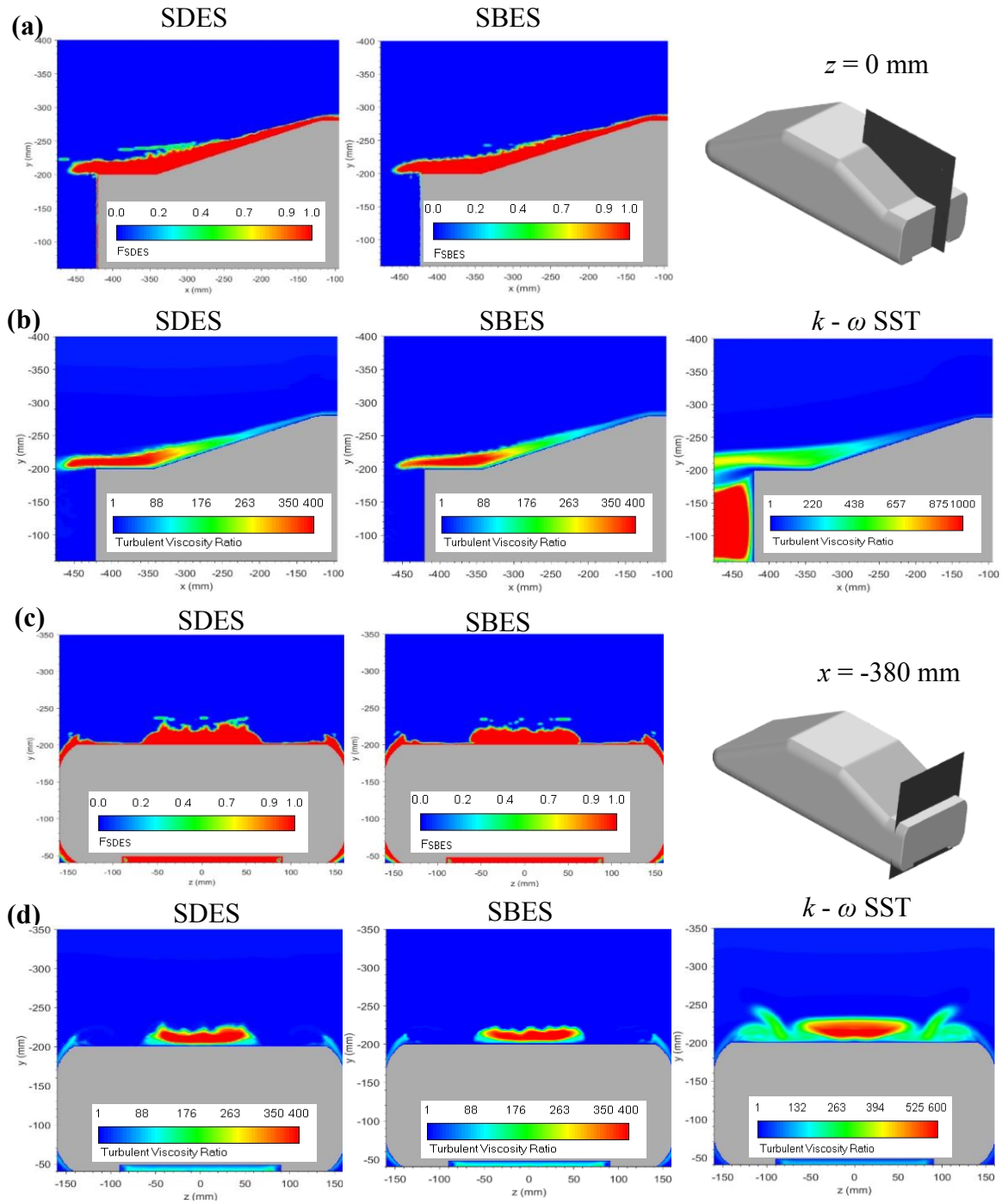

Fig. 9. Assessment of flow resolution **a), c)** Shielding function of SBES and SDES in streamwise and spanwise direction at z = 0 mm and x = 380 mm respectively, **b), d)** TVR of all the turbulence models in streamwise and spanwise direction at z = 0 mm and x = 380 mm respectively.

4.2.2. Aerodynamic force Coefficients:

The contribution of drag from each body part, such as the front slant C_{Df}, backlight C_{Dr} and base C_{Db} of the SAE T20 to the total time-averaged pressure drag $C_{D,p}$ is summarised in Table 5, whereas Table 6 represents the overall time-averaged force coefficients for SAE T20. The procedure followed for calculating the pressure drag from numerical data is presented in detail in Appendix A. The component-wise investigation of pressure drag for each component predicted by the turbulence models underpredicts the base pressure drag a maximum difference of 7.07% by $k-\omega$ SST and SDES predicts a maximum difference of 18.51% in the rear slant pressure drag. However, a more significant difference is seen to be predicted in the front slant when compared against experiment, but the pressure coefficient predicted by turbulence models on the front slant midplane shows a good agreement with experiment (Fig. 10). These differences seen may be attributed to the smaller sampling data points considered in the experiment to evaluate the pressure drag, which is apparent in the layout of pressure tapping, as illustrated by Wood (2015).

Table 5

Contribution of each body part to the total time-averaged pressure drag coefficient

Model	C_{Db}	$C_{Db}/C_{D,p}$ [%]	C_{Dr}	$C_{Dr}/C_{D,p}$ [%]	C_{Df}	$C_{Df}/C_{D,p}$ [%]
Experiment (Wood et al., 2014)	0.1053	57.4354	0.036	19.6349	0.042	22.929
$k-\omega$ SST	0.0981	72.7745	0.0306	22.7003	0.0061	4.5252
SBES	0.1005	72.0510	0.0300	21.4992	0.0090	6.4498
SDES	0.1005	72.0450	0.0299	21.4322	0.0091	6.5228

Moreover, the overall drag coefficient is underpredicted by $k-\omega$ SST, SBES and SDES by 9.14%, 9.46% and 10.3% respectively. Conversely, the overall lift coefficient predicted by all the turbulence models is less encouraging as the values predicted by the numerical simulation shows a negative lift, whereas the experiment values indicate the presence of a positive lift. The difference in lift coefficient is most likely due to the inaccuracies in the underbody flow prediction over the smooth surface of the model. Forbes et al. (2017) and Grandemange et al. (2015) have reported similar discrepancies in the lift coefficient owing to sensitivity issues. The overall difference in force coefficients reported is

mainly due to ignoring the struts, and the reported percentage of error is in line with previously published results where struts have been neglected (Aljure et al., 2014; Ashton and Revell, 2015; Guilmineau, 2008).

Table 6

Time-averaged Aerodynamic Force Coefficients for SAE T20

	Experiment (Wood et al., 2014)	***k – ω* SST**	**SBES**	**SDES**
Drag Coefficient (C_D)	0.2070	0.1889	0.1883	0.1866
Lift Coefficient (C_L)	0.0548	-0.1251	-0.1276	-0.1275

4.2.3. Pressure Coefficient (C_p) on midplane and base of the model:

The time-averaged pressure coefficient (C_p) on the mid-plane of the body is illustrated in Fig. 10. The overall pressure profile predicted by numerical simulations is in good agreement with the experimental data. Numerical simulations predict two distinctive low-pressure peaks at the leading and trailing edges of the roof, which are under-represented in the experiment. The impingement on boot-deck predicted by $k - \omega$ SST is overestimated by 5.28% whereas both SBES and SDES under predicts the impingement by 2.34% and 2.36% respectively.

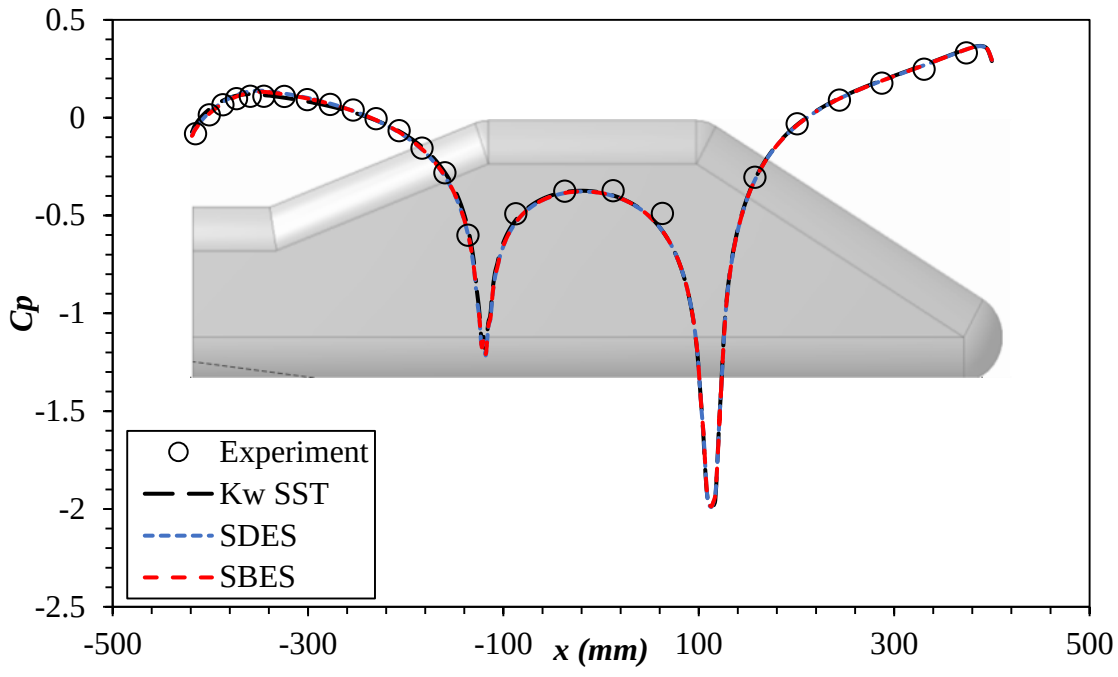

Fig. 10. Time-averaged pressure coefficient (C_p) obtained from turbulence model predictions on the midplane of the SAE T20 body compared against the experimental data (Wood et al., 2014).

The distribution of pressure coefficient (C_p) at the base of the model is illustrated in Fig 11. Both SBES and SDES predictions of overall C_p is in good agreement with experiment except at y = -90 mm where the numerical simulation predicts a higher C_p value, indicating the flow is aligned to the surface which in experiment indicates the presence of flow separation. In y = -60 mm at z = - 99.2 mm, a shift of 12.2% can be observed in the low-pressure peak between the experiment and the numerical data presented. The presence of a low-pressure region is expected as the flow accelerates over the diffuser tends to separate at the lateral edges of the diffuser, which is evidenced by the numerical simulation at z = - 89.6 mm. A subsequent effect of this separation is seen in y = 90 mm plot, where the numerical simulations overpredict the C_p value by a maximum of 15.3%. From y = -90, -120, and -150 mm, the $k - \omega$ SST predicted the flow aligned to the surface, which agrees with the time-averaged wall shear stress shown in Fig. 12.

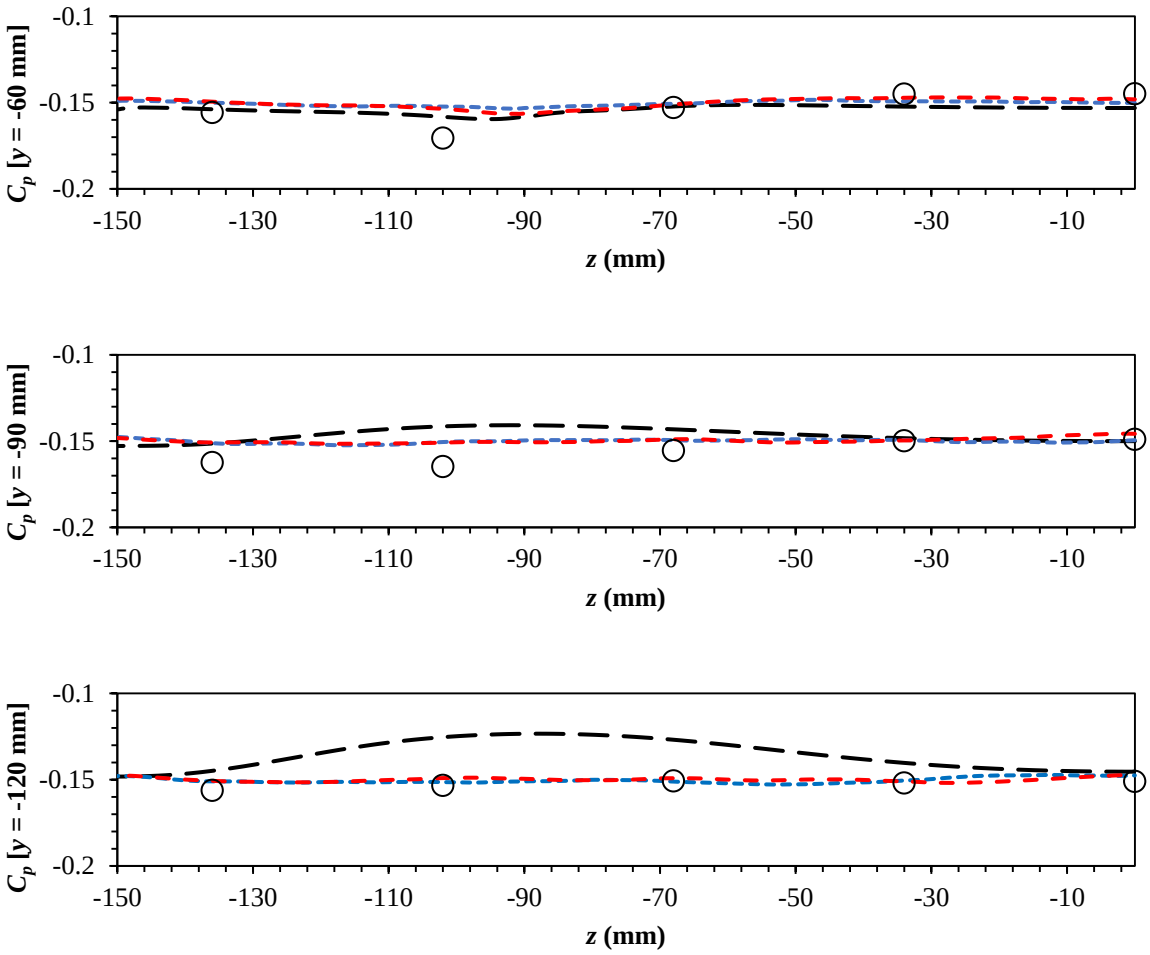

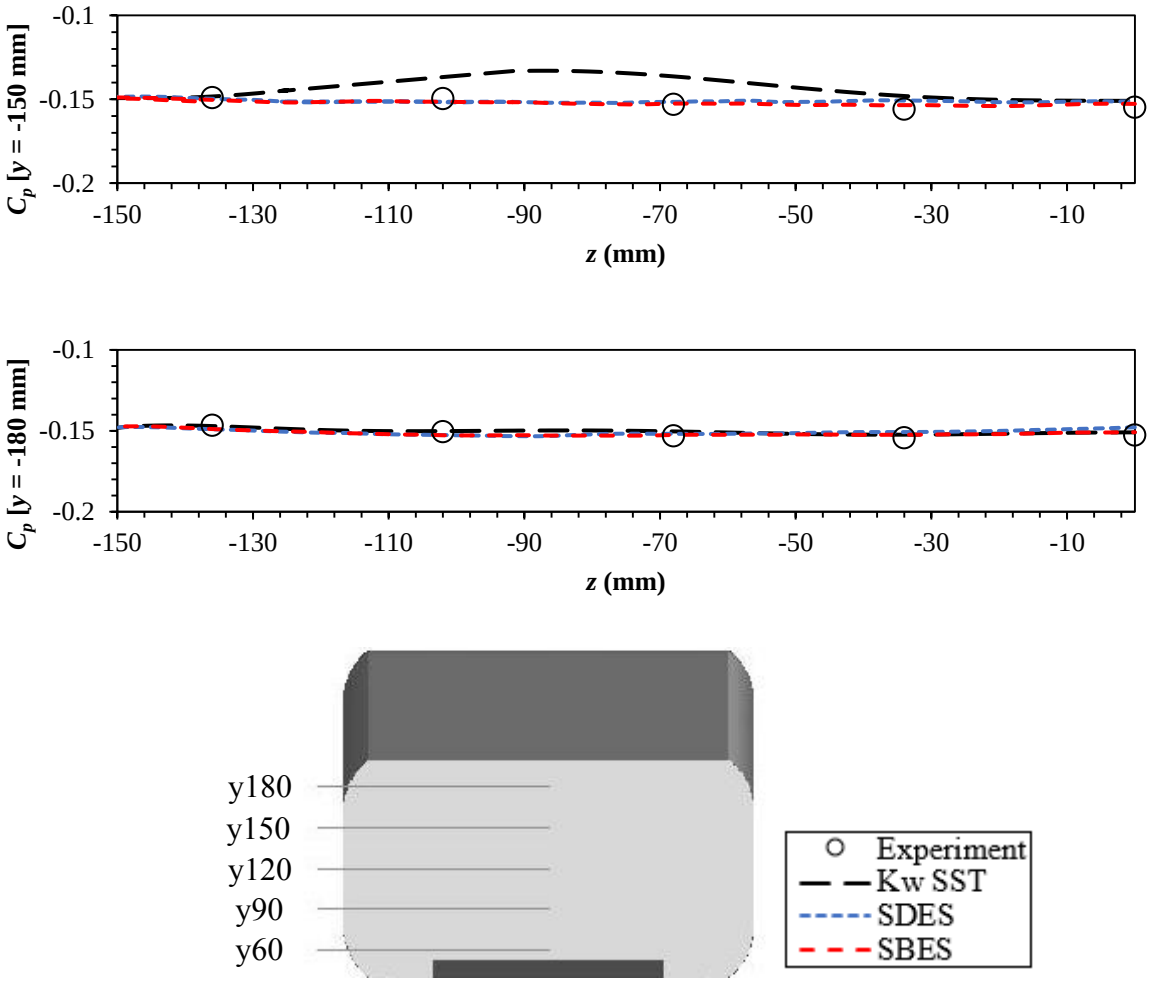

Fig. 11. Numerical predictions of the time-averaged pressure coefficients (C_p) obtained at the base of SAE T20 body compared against the experimental data (Wood et al., 2014).

4.2.4. Time-averaged Wall Shear Stress:

The flow predicted by the k – ω SST on the base of the model shows a smooth, symmetric flow pattern whereas with SBES, and SDES predicts non-symmetrical flow pattern Fig. 12. The flow over the backlight predicted by both SBES and SDES is quantitatively identical but with minor qualitative differences. The flow pattern appears to be marginally non-symmetrical in the case of SBES, but it does not translate to a strong asymmetric flow structure as seen in the experimental result (Wood et al., 2014).

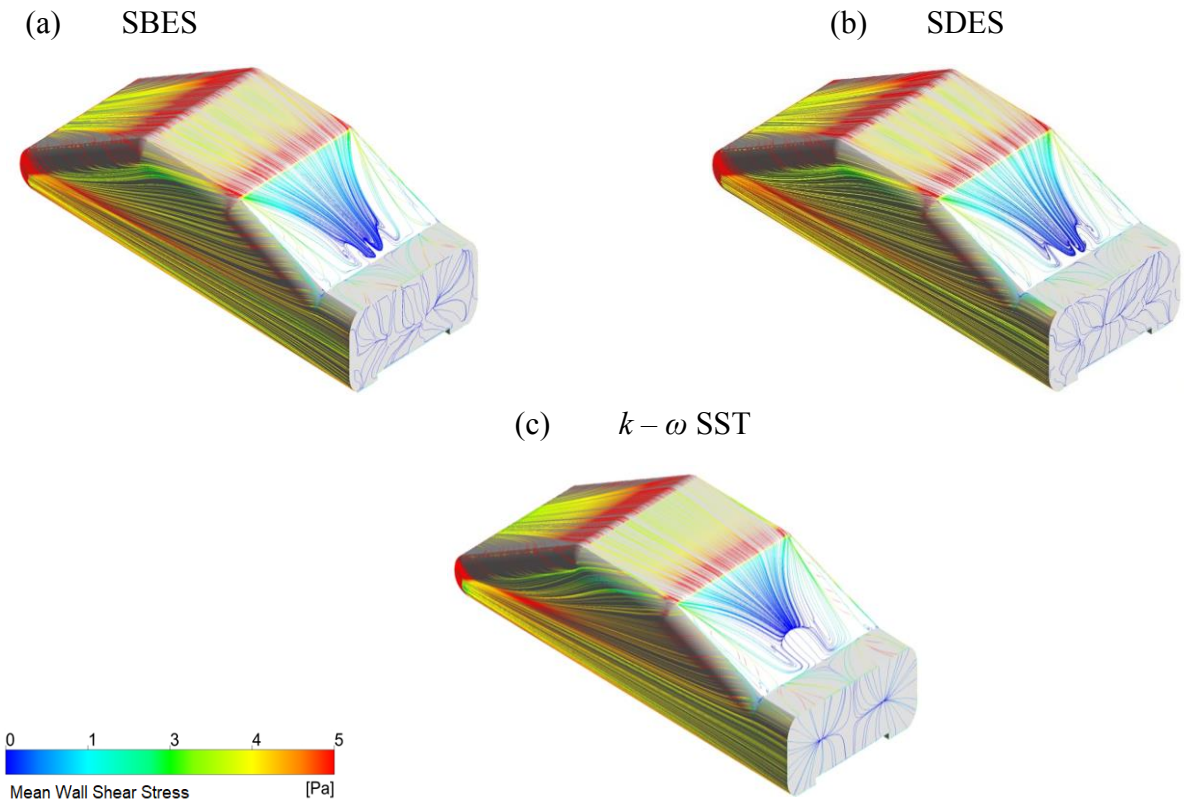

Fig. 12. Numerical predictions of the time-averaged wall shear stress (friction lines) predicted by different turbulence models on SAE T20 body.

4.2.5. Near Wake Structure:

The near wake structures predicted by numerical simulation and experimental data detail the presence of two recirculation bubbles as seen in Fig. 13. The upper recirculation bubble is formed due to the flow separation from the boot-deck, whereas the lower recirculation bubble is formed due to the flow separation from the diffuser. The upper recirculation bubble generally dominant over the lower one which tends to reduce the thickness of the lower bubble as evidenced in the experiment (Wood et al., 2014), as well as the SBES and SDES results. The centre of the upper recirculation bubble e'' is overpredicted by SBES and SDES by 1.33% and 1.9% respectively when compared to experiment whereas the $k-\omega$ SST underpredicts the results by 1.1%. The centre of the lower recirculation bubble, e' is overpredicted by SBES and SDES by 3.0% and 4.3% respectively whereas the $k-\omega$ SST underpredicts the results by 0.5%. The overall length of the near wake predicted by $k-\omega$ SST, SBES, and SDES models is overpredicted by 4.01%, 3.2%, and 1.6% respectively when compared to experiment, which agrees with the overall drag predicted by respective turbulence models.

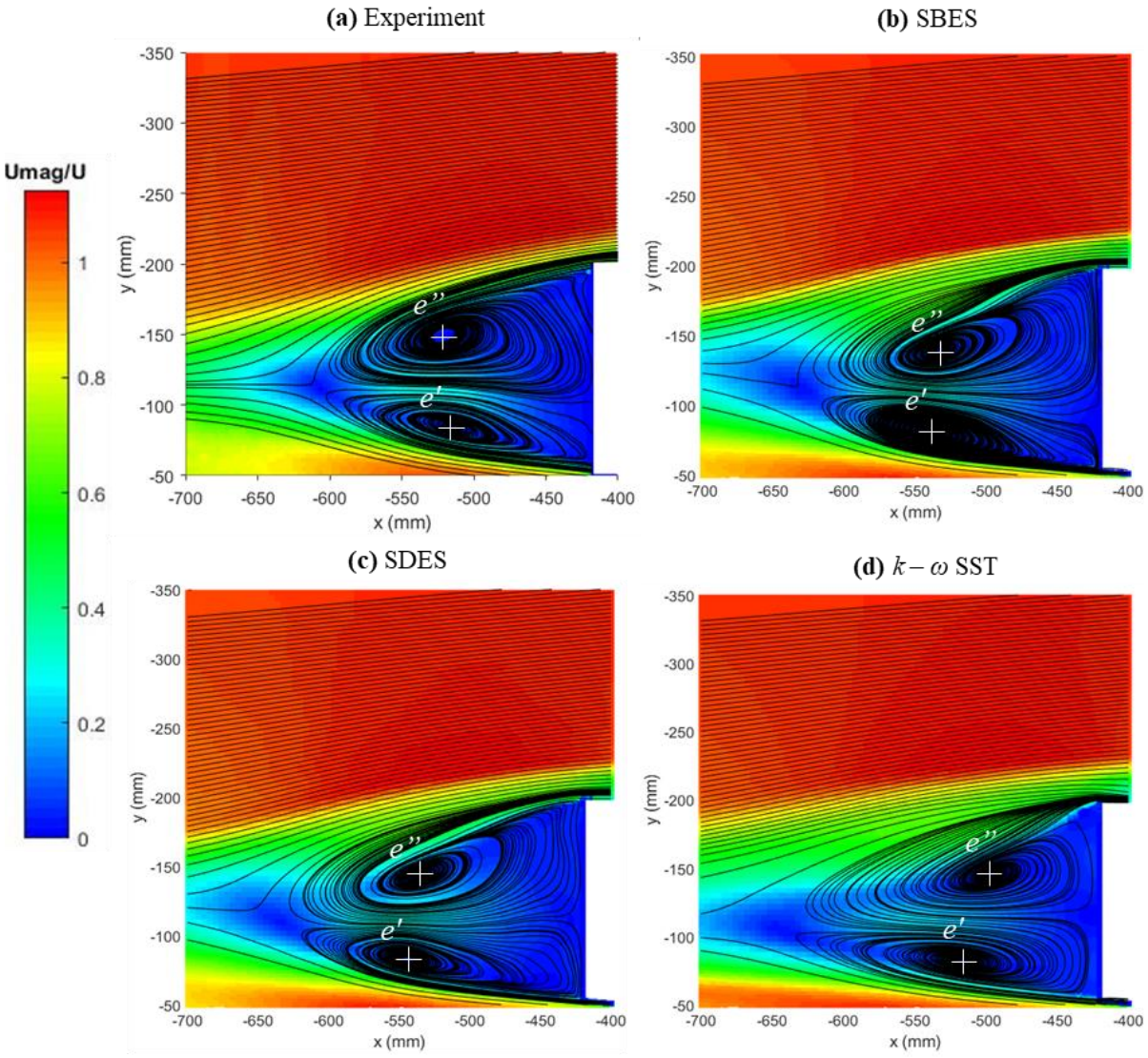

Fig. 13. Wake structure comparison of turbulence models used in the present study against experimental data (Wood et al., 2014). The centres of the upper and the lower recirculation bubbles are indicated by *e''* and *e'*, respectively.

In Fig. 14, the normalised streamwise vorticity predicted by all the turbulence models tend to show a distinctive feature when compared to the experimental data (Wood et al., 2014). The distinctive feature observed in the plots indicates two vortex zones (*a''* and *a'*) in the upper recirculation bubble which represents the two shear layers emerging from the boot-deck and the C-pillar of the notchback model which extends into the wake as evidenced in Fig. 15. Similarly, the vortex zone (*b'*) indicates a presence of shear layer emerging from the diffuser.

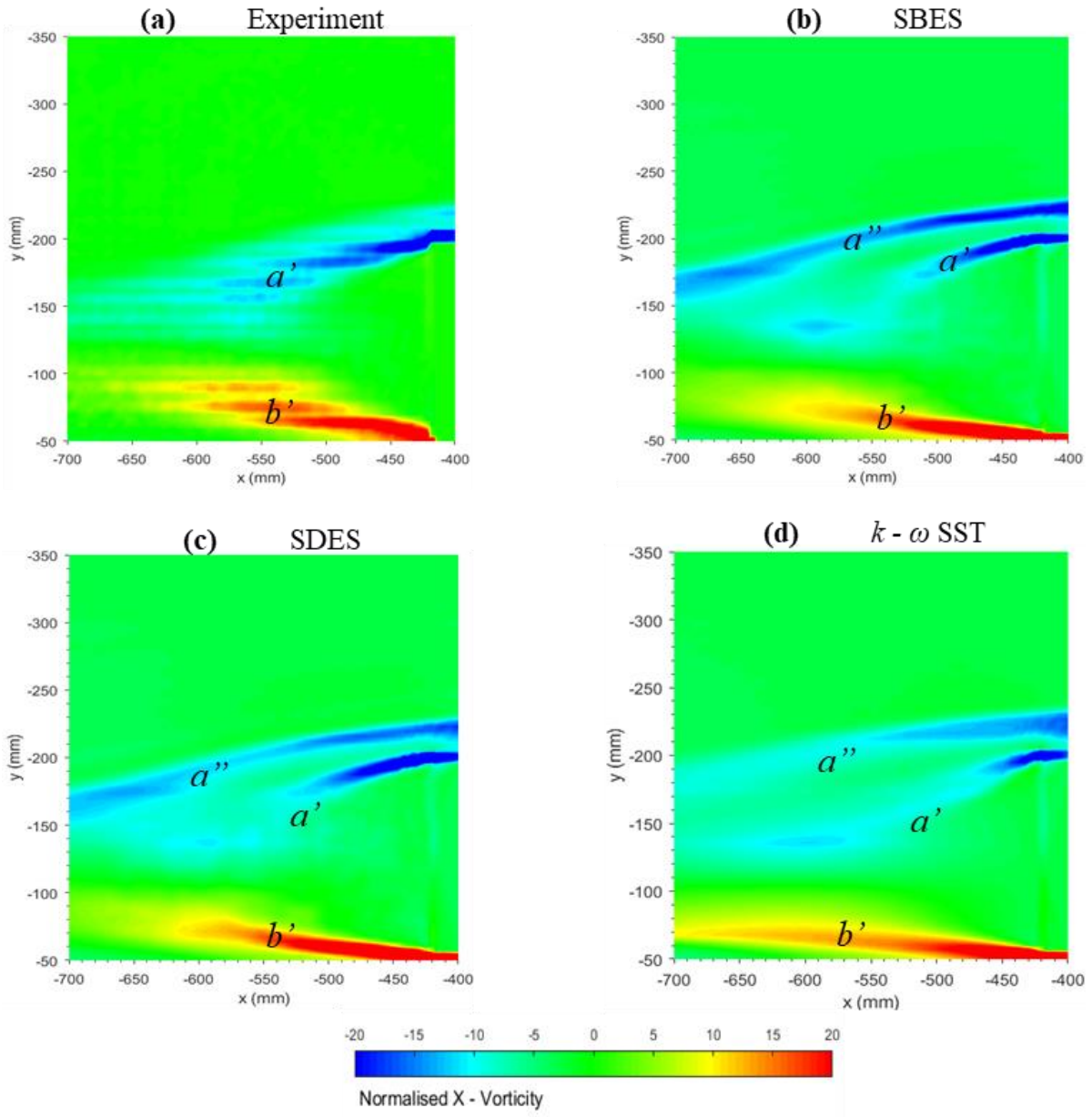

Fig. 14. Comparison of the streamwise component of time-averaged vorticity predicted by turbulence models used in the present study with the experimental data (Wood et al., 2014).

4.2.6. Streamwise Velocity Profiles:

A comparison of the velocity profiles is plotted in the wake of the body and at various locations in the plane of symmetry, as shown in Fig. 15. The experimental data indicates the presence of strong separation on the backlight, which is evident from x = -190 mm; this grows downstream and impinges just after x = -340 mm. However, such strong separation is not predicted by any of the turbulence models used in the current study.

The velocity profiles in the wake of the body show that all the turbulence models predict a shear layer which starts at x = -460 mm and grows as it moves away from the body

which influences the lower recirculation bubble to be squeezed, as seen in the streamline plots in Fig. 13. As the shear layer grows into the wake of the body at x = -620 mm the velocity profile predicted by all the turbulence models follow the trend of the experimental data, but the streamwise velocity is overpredicted due to absence of struts resulting in smooth underbody flow. As a result, the length of the lower recirculation bubble is overpredicted, as seen in Fig. 13.

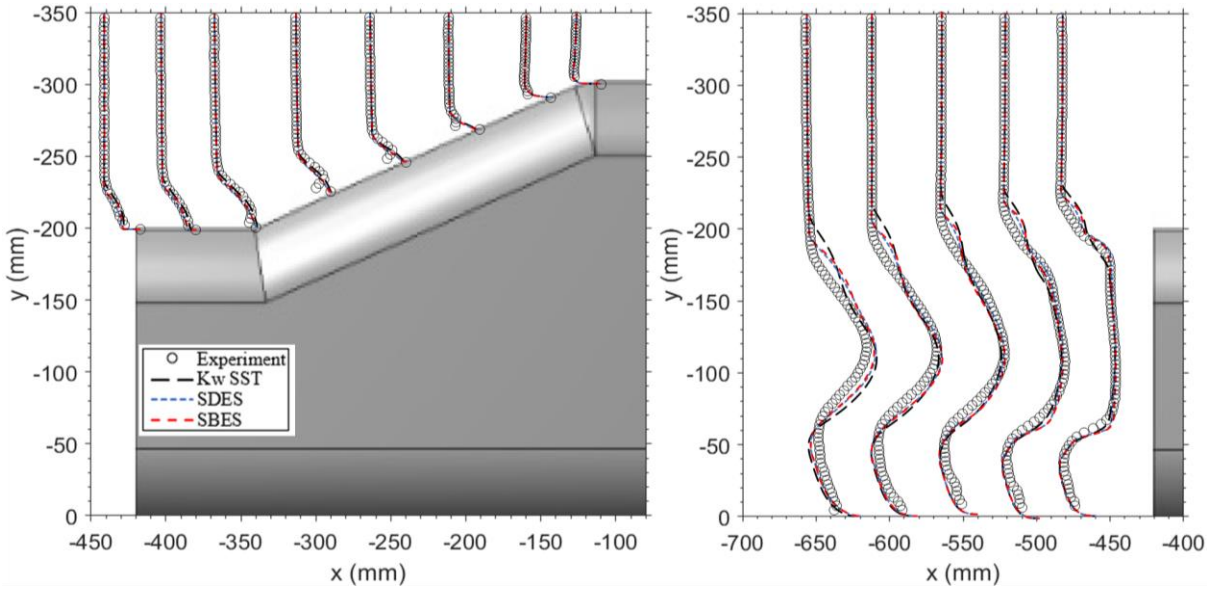

Fig. 15. Predictions of the normalised, time-averaged streamwise velocity profiles from different turbulence models at several locations compared against the experimental data (Wood et al., 2014).

4.2.7. Spanwise and Streamwise Velocity Contours:

The time-averaged normalised velocity magnitude (U_{mag} = U_{mean}/U_{∞}) behaviour on the spanwise velocity contours from x = -190 mm to -420 mm is illustrated in Fig. 16. At x = -190 mm, the experimental data shows there is no flow separation, whereas SBES and SDES predicts a slight flow separation but, $k-\omega$ SST predicts the flow separation distinctly, as seen in Fig.16. Moving downstream to x = -240 mm it is observed that all the turbulence models predicted flow separation with $k-\omega$ SST showing a stronger separation region in contrast to experimental data where there is no flow separation. At x = -290 mm, the experimental data reports a recirculation bubble which is in line with the velocity profile prediction in Fig. 15.

Interestingly, the experimental data reports a non-symmetric flow structure, which moving further downstream is most visible at x = -420 mm. In Fig. 16, it is evident that the SBES and SDES models predict a strong C–pillar vortex structures at x = -290 mm and -340 mm, which appear to be weaker in the experimental result. The velocity contours from the SBES and SDES show a negligible difference between them but differ from $k-\omega$ SST. In the

case of $k - \omega$ SST, flow structures on the backlight and boot-deck appear symmetrical whereas, with SBES and SDES cases, the non-symmetric flow that is predicted is weak as previously shown in Fig. 12 and with a little more clarity in Fig. 9c & d. Additionally, the apparent non-symmetric behaviour of the SSL in the experimental result is further detailed in Figs. 17 and 18, which show a series of vertical planes across the width of the body between the two counter-rotating vortices; namely, z = 60 mm and –60 mm. Due to the interaction of the flow from the side with the flow from the roof of the body, a weak backflow is observed at z = –30 mm in the experimental data shown in Fig. 18. Nevertheless, such an effect is not predicted by any of the turbulence models examined in this study.

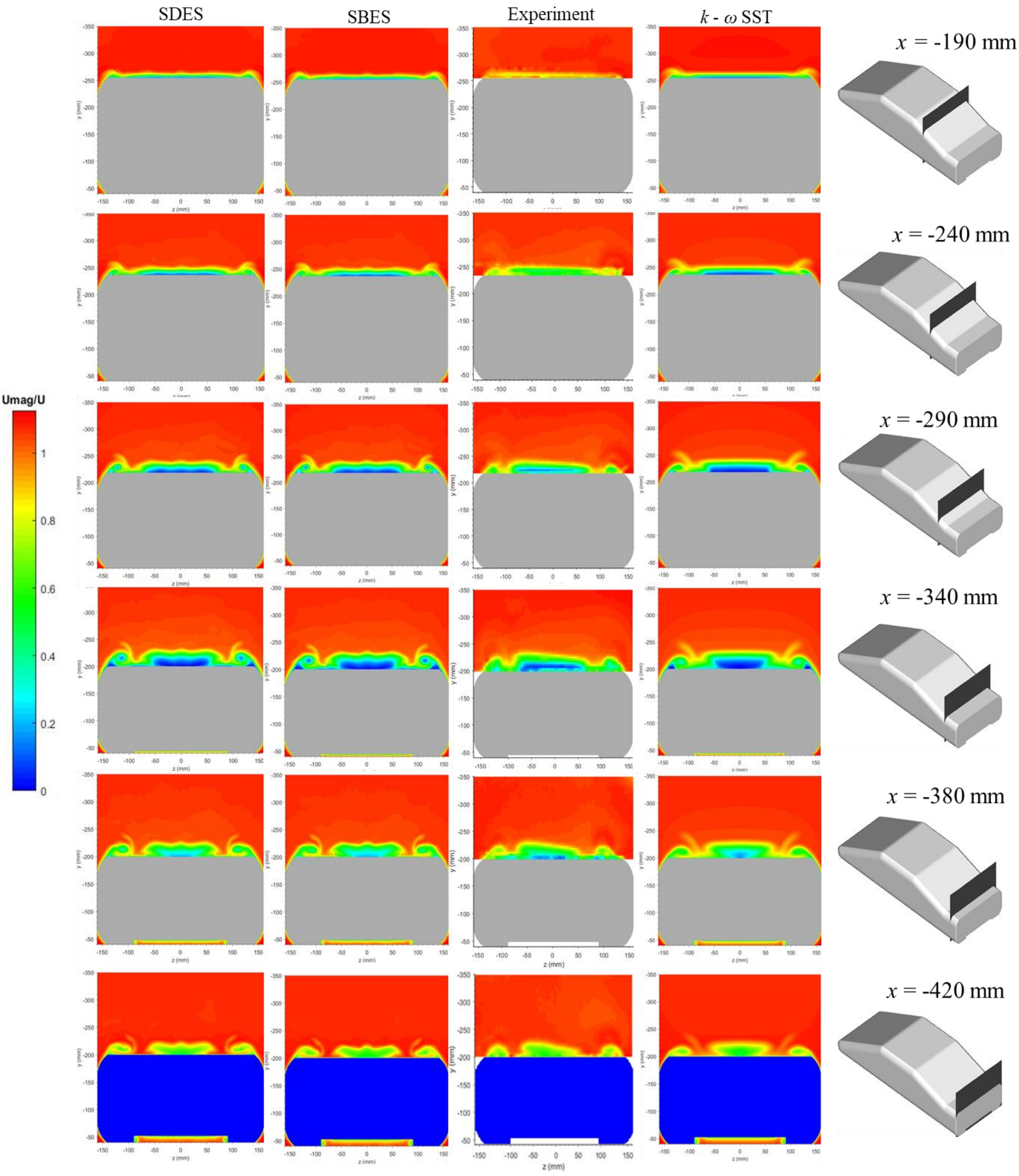

Fig. 16. Normalised time-averaged velocity magnitude contours compared with the experimental data (Wood et al., 2014). From top to bottom each row corresponds to the locations x = -190 mm, -240 mm, -290 mm, -340 mm, -380 mm and -420 mm respectively.

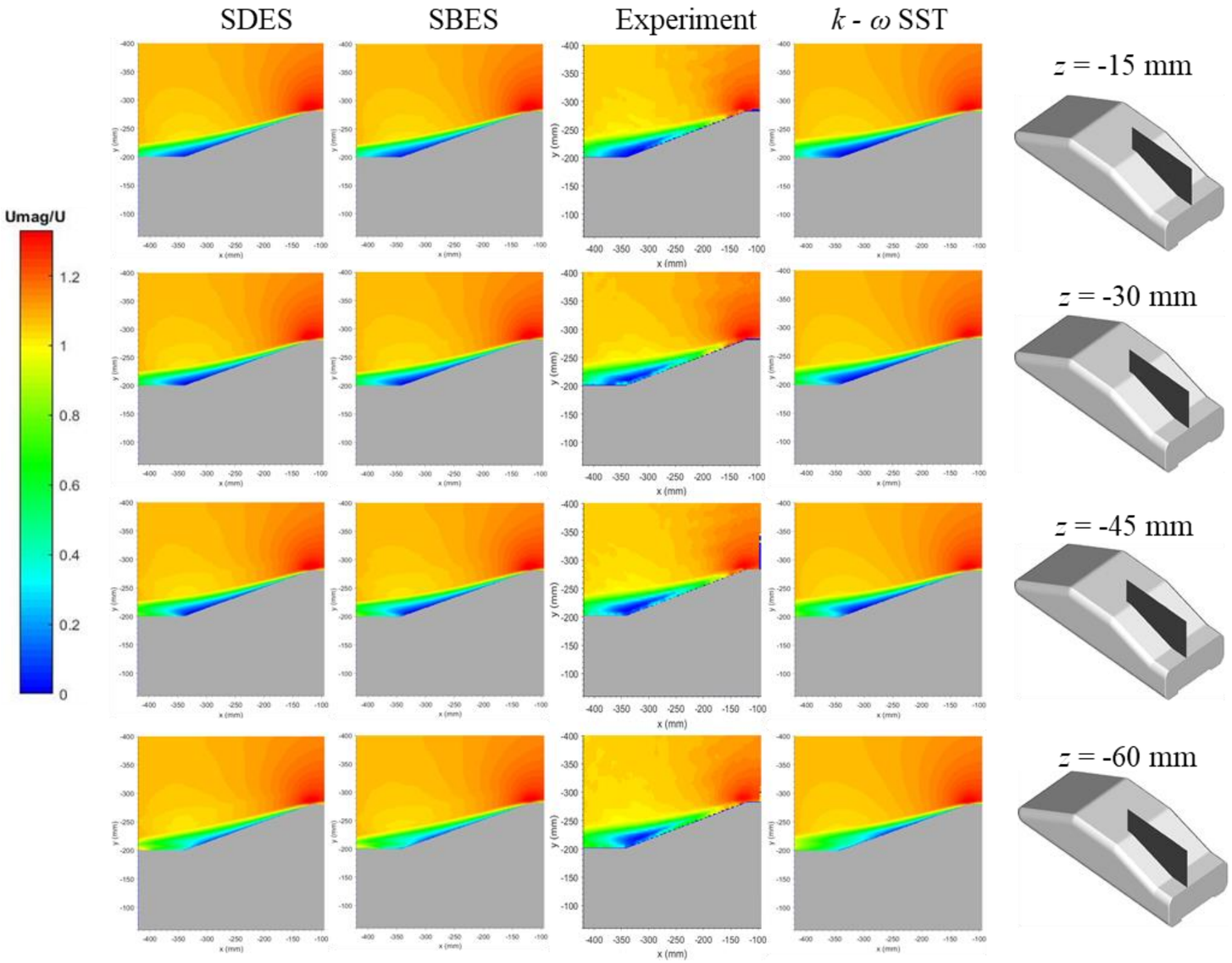

Fig. 17. Normalised time-averaged velocity magnitude contours compared with the experiment (Wood et al., 2014). From top to bottom the row correspond to the locations z = -15 mm, -30 mm, -45 mm and -60 mm respectively.

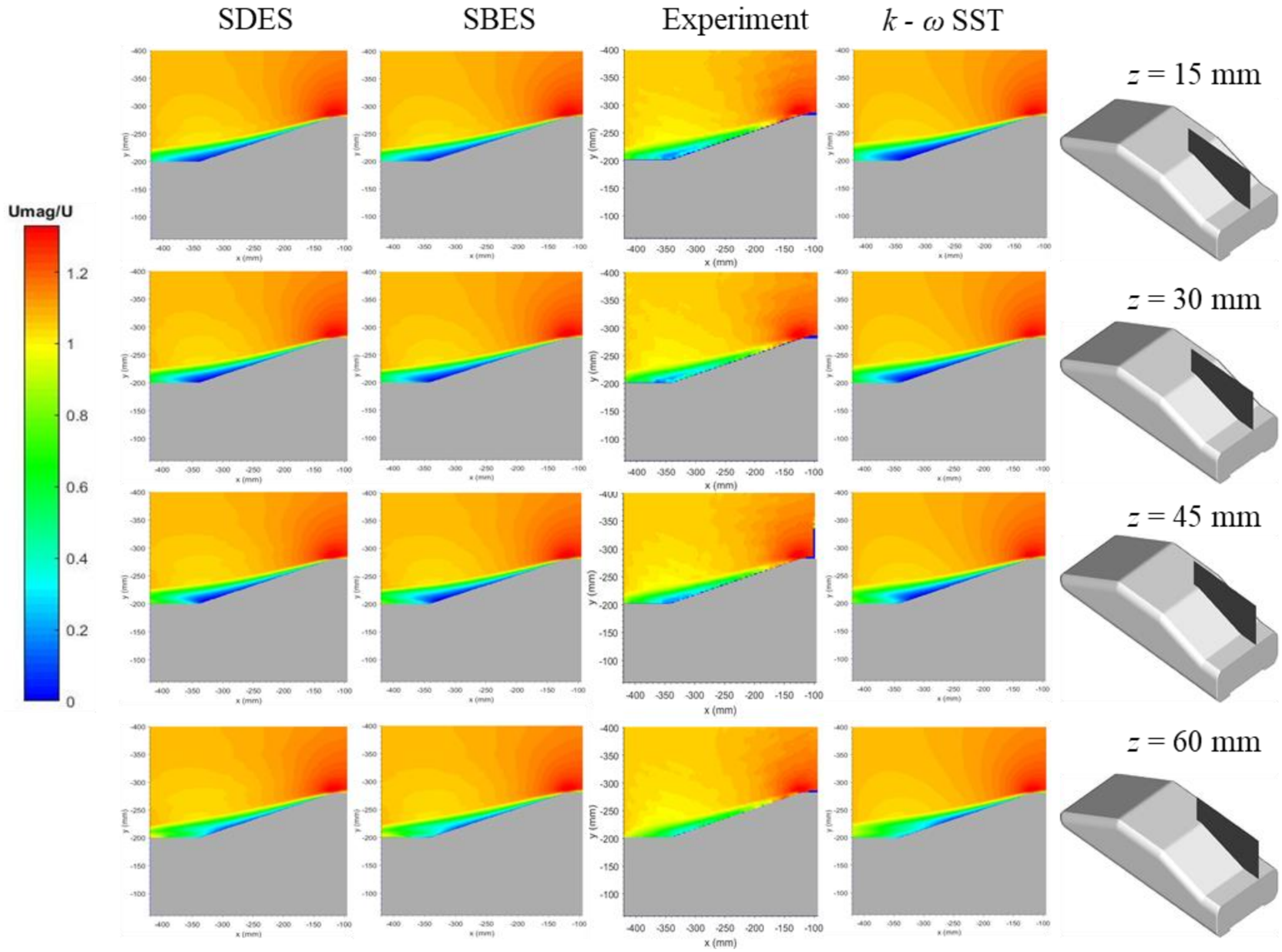

Fig. 18. Normalised time-averaged velocity magnitude contours comparison with experiment (Wood et al., 2014). From top to bottom the row correspond to the locations z = 15 mm, 30 mm, 45 mm and 60 mm respectively.

4.3. Influence of backlight angle:

4.3.1. Near Wake Structures and Aerodynamic Force Coefficients:

From Fig. 19, it is evident that the change in backlight angle results in a decrease in the length of the recirculation bubbles and increase the flow reattachment to the base of the body. As the backlight angle increases from 20° to 30°, the flow separated from the backlight impinges close to the edge of the boot-deck. However, the numerical results predict weak or no impingement of the flow on the boot-deck for 40°, as seen in Fig. 21(b), leading to a larger upper recirculation bubble to form closer to the base of the model which increases the drag. We, therefore, see that the SAE T40 presents as a higher drag configuration amongst that investigated (Table 7). Interestingly, we find that the drag coefficient is underpredicted by 9.46% and 10.3% by SBES and SDES for SAE T20 whereas it is overpredicted for both SAE T30 and T40 by 1.75% and 1.5% by SBES and 3.32% and 1.9% by SDES respectively when compared against experimental data (Wood, 2015).

Table 7

The time-averaged drag coefficient predicted by the numerical models for various backlight angles (θ) compared with experimental data (Wood, 2015).

Backlight Angle (θ)	**Experiment** (Wood, 2015)	**SBES**	**SDES**
20°	0.207	0.1883	0.1866
30°	0.260	0.2646	0.2688
40°	0.284	0.2883	0.2895

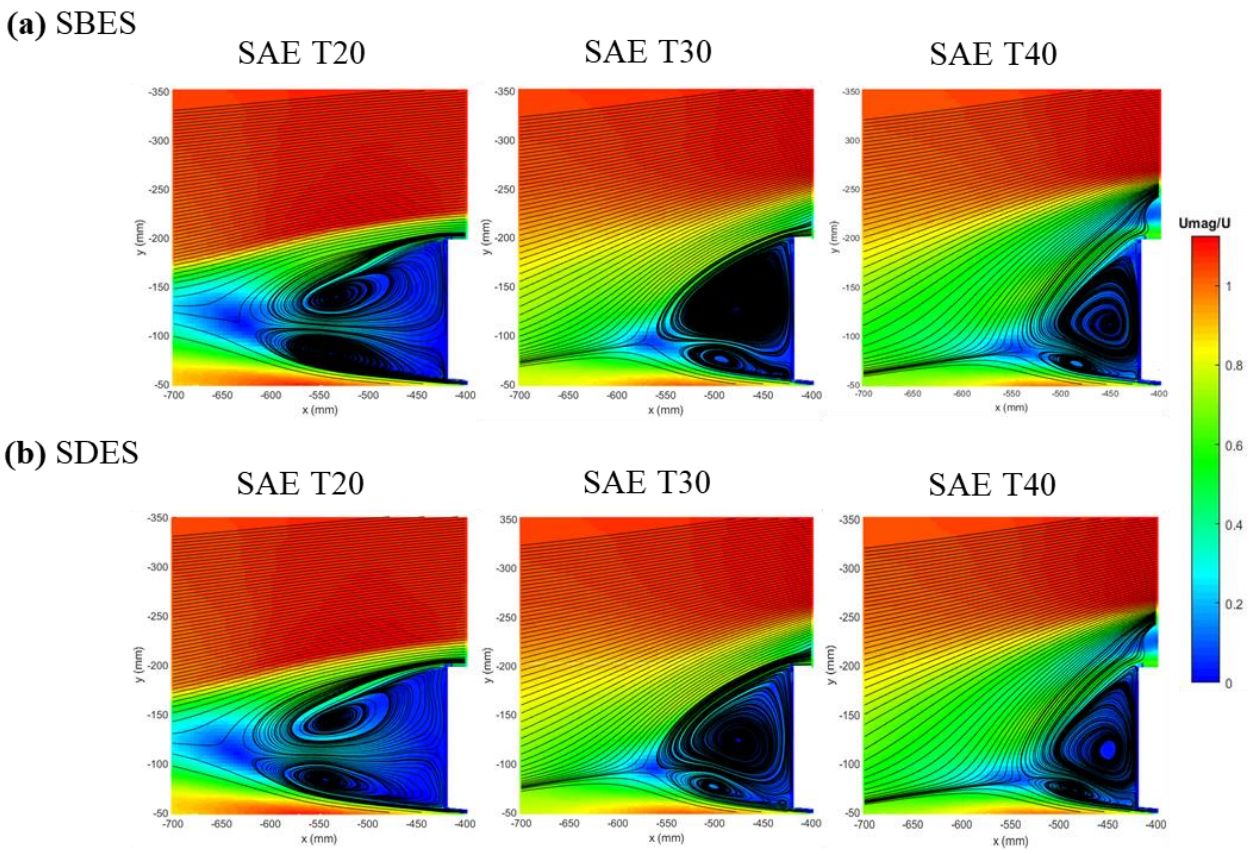

Fig. 19. Time-averaged Streamline plots on symmetry plane of SAE reference body with three different slant angles of θ = 20°, 30°, and 40°predicted by the SBES and SDES models.

4.3.2. Spanwise Velocity Contours:

Time-averaged velocity magnitude on spanwise planes shows a growth in the SSL as the backlight angle increases (Fig. 20). At the outset, it is evident from Fig. 20 (a) and (b) that there are no considerable differences between the flow features predicted by the SBES and SDES. For SAE T30 and T40 configurations, the turbulence models predict a non-symmetrical flow behaviour on the planes plotted in Fig. 20, which is in agreement with the observation made by Wood (2015). In the case of SAE T30 and T40, the trailing vortex on the right appears to be merged with the flow separated from the leading edge of the backlight. Whereas on the left side, the vortex structure weakens in SAE T30 and vanishes in SAE T40 as seen in Fig. 20. In the experiment, it is observed that the weakening of the trailing vortex is the cause for the flow to be non-symmetrical (Wood 2015).

Considering that there are negligible differences between the SBES and SDES models, from this point onwards, we shall present the numerical results obtained from the SBES model for different backlight angles.

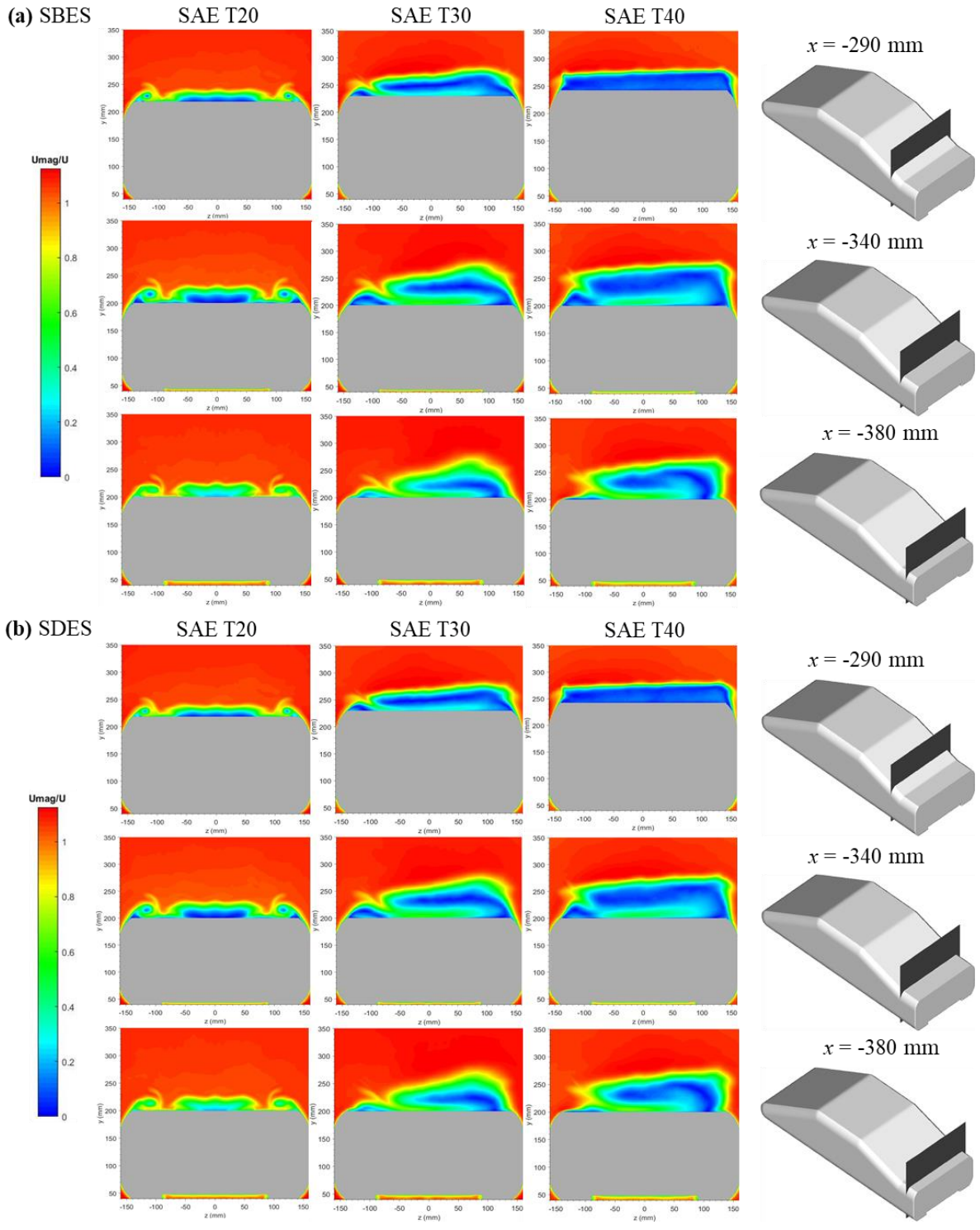

Fig. 20. Time-averaged velocity magnitude on spanwise planes at x = 290 mm, 340 mm and 380 mm respectively for various SAE reference body with three different slant angles of $\theta = 20^0$, 30^0, and 40^0 predicted by *SBES* and *SDES* models.

4.3.3. Wall Shear Stresses over the Backlight:

Fig. 21 illustrates the flow behaviour on the surface of the vehicle using time-averaged wall shear stresses. In SAE T20, a pair of trailing vortices is seen to emerge from

the leading lateral edges of the backlight at point *b*. These free shear layers traverse downstream along the line *c* and impinge on the boot-deck, which lead to an increase in the pressure at the intersection of backlight and boot-deck as seen in Fig. 22(a). The direction of rotation of these vortices is marked by *d*. The flow separated from the backlight is seen to be squeezed towards the centreline of the model due to the presence of these vortex structures. The region of flow separated on backlight is marked by *a*, and the direction of the flow within this region is marked by *k* and *l*. The secondary flow structures marked by *e* are predicted on the lateral edges of the backlight, representing stagnation zones. The vortex structures that impinge along *c* on the boot-deck flow towards the centreline (*i*) along the directions *f* and *g* respectively, which result in parting line *h*. The prediction of line *h* from numerical simulation lies close to the centreline. However, in the experimental data (Fig. 21(b) – SAE T20) indicates that the parting line *h* is offset from the centreline due to the difference in the strength of the trailing vortices. This difference results in the formation of a small region of separated flow (*j*), which contributes to the non-symmetrical flow behaviour on the backlight. Such a feature is not predicted by numerical simulation.

As the backlight angle is changed to 30°, the predicted flow pattern changes, giving a non-symmetrical flow behaviour on the backlight. The separated region *a* has grown in size when compared to SAE T20, and the negative pressure it induces across the backlight (Fig. 22(a)) contributes to an increase in overall drag as seen Table 7. The flow in this region rotates about points *b* and *c*. The stronger vortex *b* governs the direction of flow (*j*) and moves the flow upwards covering most of part of the backlight. Points *b* and *c*, being closer to the lateral edges of the backlight, influences the formation of vortex structures as the point being closer to the leading edge of the backlight draws the flow into *b* and on the other side into *c*. Usually, these vortices are expected to roll-up to form a roughly symmetric trailing pair vortex as seen in Fig. 21(a) – SAE T20. Interestingly, a reattachment line *d* is seen on the lower half of the backlight, indicating the presence of weak trailing vortex-like structures as seen in Fig. 20. However, on the other side, there is no presence of such vortex structures.

Further, the direction of flow (*k*) at *c* is in the opposite direction as predicted at *b*, which results in the formation of a parting line *g*. On the boot-deck, the direction of flow rotation in the region *a* is strong, which influences the flow on the boot-deck to move up the backlight leading to the formation of another parting line, *n*. Further downstream, the flow tends towards the edge of the boot-deck in direction *l* and *m*. However, for the SAE T30 configuration, the differences between the model results and experimental data are noticeable

especially with respect to the strength of the rotation of flow in the separated region *a*, formation of counter-rotating vortices, and the secondary flow structures shown in Fig. 21(b) – SAE T30. In the separated region *a*, the experiment recorded that the flow rotating around point *c* is stronger than the rotation of flow at *b*, and location of *c* is further away from the lateral edge of the backlight which allowed the formation of a low strength trailing vortex on the right side of the model.

In SAE T40, it is evident that there is a dominating primary vortex emerging from the left side of the model, which grows towards right-side covering most of the backlight, thus showing a strong non-symmetrical flow behaviour. The direction of the flow in the vortex marked by *a* indicates that the flow is being driven up the backlight and because of its strength, there is a flow stagnation marked by region *b*. The presence of the vortex results in the pressure approaching a minimum on the edge of the backlight, as seen in Fig. 22(a), resulting in a higher drag coefficient (Table 7). The stagnated flow then drains on the right side of the model following *c*. The presence of small secondary rotating structure, *d* can be seen on the right side of the model; however, the faint friction lines indicates that this structure to be weak or unstable. On the left side of the model, the flow tends to rotate around node *e* and attaches to the boot-deck marked along with the line *g*. The reattachment of this rotating flow on the boot-deck results in a high-pressure zone on the boot-deck, as seen in Fig. 22(a). The presence of another flow stagnation *f* can be seen as a result of the strong primary vortex *a* and secondary flow rotation at *e*. In the experimental data, the primary vortex tends to align with the centreline of the model as Fig. 21(b) – SAE T40 as it passes over the boot-deck, whereas no such alignment is seen in the numerical prediction. As a result, the secondary vortices *d* and *e* predicted by the numerical result appear mitigated and smaller in size.

In summary, while there are apparent differences between the experimental oil-flows and model predictions of time-averaged wall shear stresses, there are still a number of points of commonality that the model can predict, even if the separation lines and vortex cores are displaced in comparison with experiments.

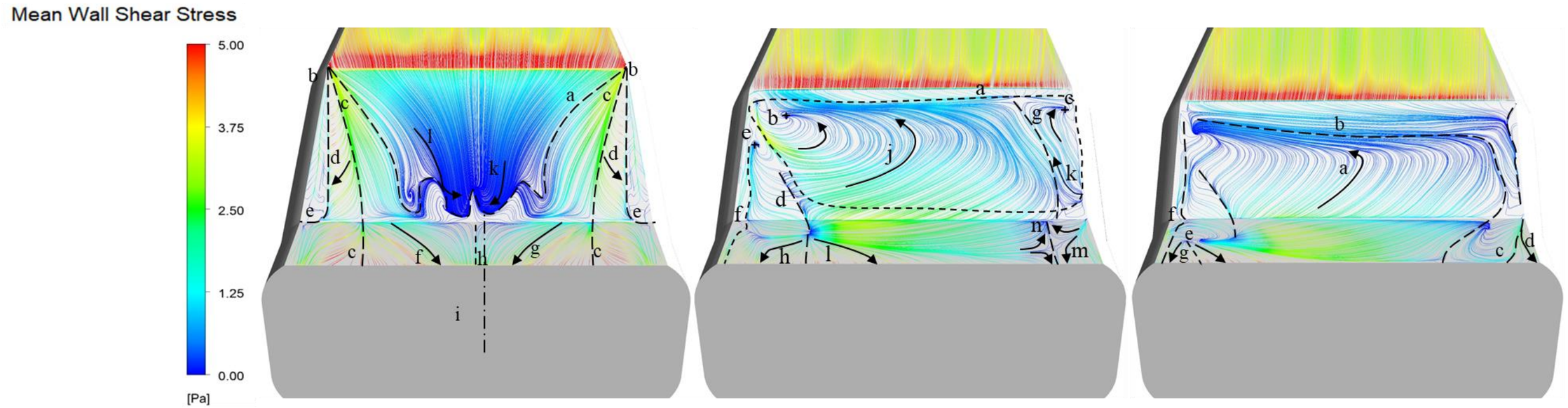

Fig. 21. Time-averaged values of **a)** Wall shear stresses (Friction lines) and **b)** Experimental results[1] (Oil flow) presented by Wood (2015), plotted on the rear of the model for all the backlight angles used in this current study.

[1] The experimental images are used are in line with Creative Commons (CC) License agreement and authors fully-acknowledge both the Author Dr Daniel Wood and Loughborough University.

4.3.4. Pressure Coefficient on the backlight:

The impingement region predicted by numerical simulations is in agreement with the experiments for all the cases investigated, as seen in Fig. 22. The points *b* and *d* represents the impingement points in SAE T20 and SAE T30, whereas the impingement region is represented by *c* for SAE T40. The intensity of pressure predicted at the impingement region is seen to decrease with increase in the backlight angle, and the location of the impingement point moves closer to the edge of the boot-deck as observed in experiments. In the case of SAE T30, the low-pressure region predicted for SAE T30 and T40 and the pressure predicted on the backlight for SAE T20 shows a reasonable agreement with experiments. The predicted pressure at the backlight (Fig. 22b) for both the SAE T20 and T30 bodies is higher than the measured values, although the predicted pressure gradient is reasonable. Conversely, the prediction of the actual separation points on each of the bodies correlates quite well to the experimental measurements, which is also seen in Fig 17. & 18 for SAE T20.

The generation of the lateral vortex from the middle of the backlight represented by *b*, and impingement of the vortex along the line *e* is well predicted by numerical simulation for SAE T30 as seen in Fig. 22. However, the location of line *e* appears to be closer to the primary vortex, which contributes to the massive impingement zone on the boot-deck. For the case of SAE T30, the low-pressure region (*a*) predicted by numerical simulation is lower in intensity than that observed in the experiments and the pressure at the impingement region at the boot-deck is overpredicted by the model highlighting apparent quantitative differences with the experimental data. The differences in the pressure intensity can be attributed to the local flow behaviour on the curvature of the model and the lateral edge of the backlight, as shown in Fig. 21a. Although the overall agreement between the model and experiment appears to be reasonable for the case of SAE T40, the experimental results indicate the presence of a weak trailing vortex closer to the boot-deck and backlight interaction which is less accurately predicted by the model as seen in Fig. 23c. The low-pressure region on the backlight of SAE T30 and T40 tends to recover across the mid-plane, evidenced in both numerical and experimental results and this agreement appears to be reassuring.

Further, the contribution of the total time-averaged pressure drag coefficient of each body part for SAE T20, T30 and T40 in comparison to the experimental data is summarised in Table 8.

Table 8

Comparison of component-wise pressure drag predicted for 20°, 30°, and 40° backlight angle.

θ	**Model**	C_{Db}	$C_{Db}/C_{D,p}$ [%]	C_{Dr}	$C_{Dr}/C_{D,p}$ [%]	C_{Df}	$C_{Df}/C_{D,p}$ [%]
20°	Experiment	0.1053	57.4354	0.036	19.6349	0.042	22.929
	SBES	0.1005	72.0510	0.0300	21.4992	0.0090	6.4498
30°	Experiment	0.1151	45.9283	0.0898	35.8306	0.0457	18.2410
	SBES	0.1094	52.6468	0.0936	45.0433	0.0048	2.3099
40°	Experiment	0.1224	44.9775	0.1004	36.8816	0.0494	18.1409
	SBES	0.1152	52.1267	0.1029	46.5611	0.0029	1.3122

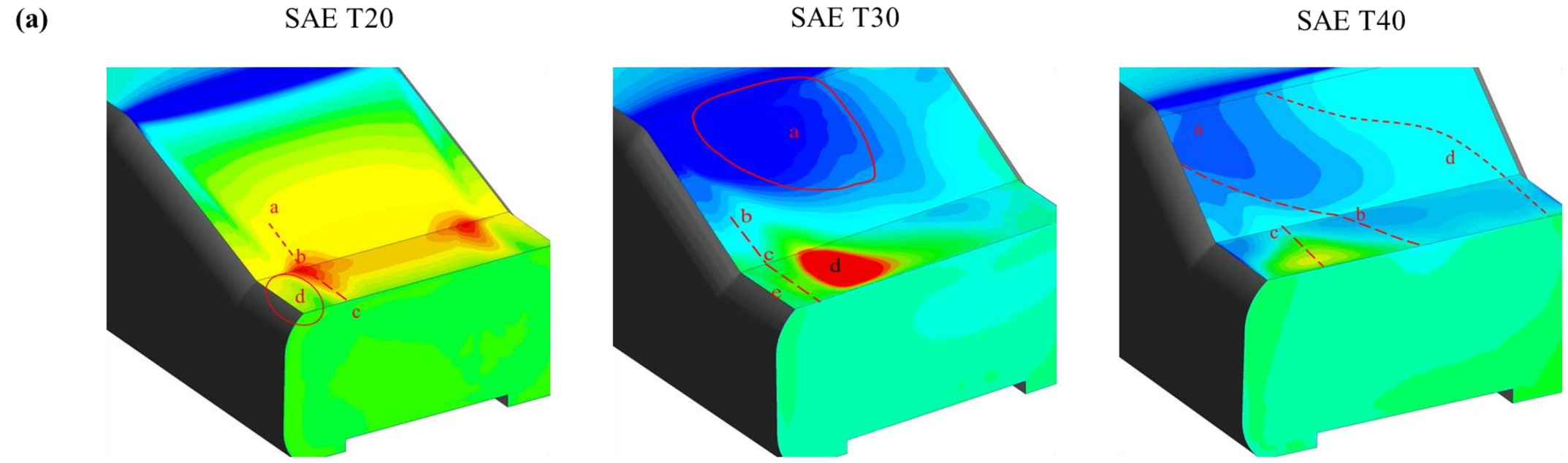

Fig. 22. Time-averaged values of **a)** pressure coefficient predicted by numerical simulation and **b)** Experimental pressure coefficient results[1] presented by Wood (2015), plotted on the rear of the model for all the backlight angles used in this current study.

[1] The experimental images are used are in line with Creative Commons (CC) License agreement and authors fully-acknowledge both the Author Dr Daniel Wood and Loughborough University.

4.3.5. Trailing Vortex Structures:

In Fig. 23, *a′* and *a″* show the trailing vortices generated from the leading edges of the backlight, whereas *c′* and *c″* indicate the longitudinal vortex structures formed from the sides of the model. The size of these vortices increases when the trailing vortices merge downstream. A transverse vortex *b′* is seen to form behind the backlight angle between the two trailing vortices on either side of the model. In SAE T20, this transverse vortex is seen to be squeezed between the two trailing vortices because of the strength of these vortices being equal. With the increase in backlight angle to 30°, the trailing vortex *a′* tends to merge with transverse vortex *b′* because of the difference in the strength of the vortex as seen in Fig. 23(b). On the other side, *a″* is seen to emerge from the lower half of the backlight, which is due to the presence of the flow rotating around node *b*, as seen in Fig. 21. The transverse vortex downstream merges with *c′* and increases its length when compared to *c″*. A further increase in the backlight angle to 40°, results in similar behaviour with an increase in the size of *c′* vortex is also seen in Fig. 23(c). Interestingly, it appears that there is no presence of the trailing vortices *a″* and *a′*, emerging from C-pillars as they merge fully with the transverse vortex (*b′*) leading to a strong non-symmetrical flow behaviour.

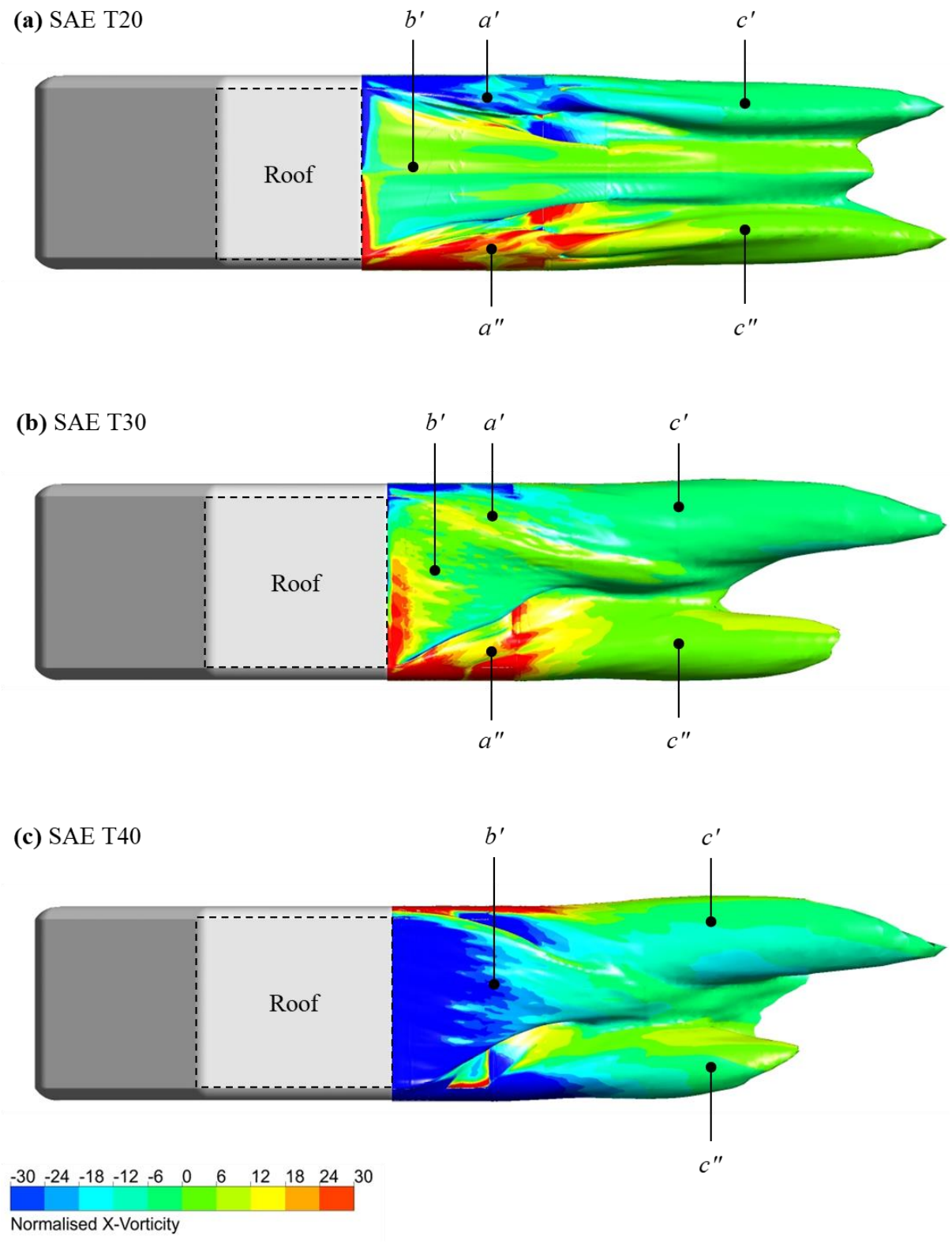

Fig. 23. Iso surface of time-averaged velocity magnitude (30 ms^{-1}) coloured with normalised time-averaged x vorticity for all the backlight angles investigated.

5. Summary and Conclusions:

An investigation of Scale Resolving Simulations was conducted for evaluation of salient features of a notchback model with different turbulence models and then backlight angles. Initially, the SBES and SDES models were assessed alongside with the URANS based $k - \omega$ SST model to understand the flow resolution better on an unstructured mesh based on hybrid RANS-LES recommendations for an SAE reference body with a 20° backlight. An overview of the turbulence model formulation and the setup conditions were discussed. A grid resolution study was conducted through a systematic approach to achieve a mesh that is capable of resolving flow features up to the Taylor microscale on the backlight. Within the turbulence models investigated in this study, both SBES and SDES showed enhanced capabilities in resolving flow features when compared to the standard URANS model. However, qualitatively SBES appears to resolve the internal flow structures marginally better than SDES. Within the scope of this study, for a 20° backlight angle, none of the turbulence models investigated was capable of predicting the non-symmetric flow behaviour as reported in experimental data by Wood (2015) and Wood et al. (2014). However, SRS models predicted the pressure distribution and aerodynamic force coefficients with good agreement to the experimental data overall. Furthermore, the transition from RANS to LES was more rapid and definitive for SBES when compared to SDES.

The influence of the backlight angle on the flow features around the notchback geometry was investigated using both SBES and SDES. The change in the backlight angle increases the drag force experienced by the model as the location of impingement of flow on boot-deck influences the size of the near wake structures. The SSL is seen to grow into the wake with an increase in backlight angle, which influences the impingement of the flow on boot-deck. It was observed that with the increase in the backlight angle, the general flow features become more non-symmetric due to the reduction in strength of the trailing vortex structures on one side of the geometry and compensated by enhancing on the other side. In summary, we find that the influence of change in backlight angle showed a tendency to alter the strength of the C-pillar trailing vortex owing to which non-symmetrical flow feature is seen.

Acknowledgement:

The authors would like to thank Professor Martin Passmore and Dr Daniel Wood of Loughborough University for sharing their experimental data by providing open access to their repository. Additionally, the authors would like to thank ANSYS for the Academic Research Partnership Grant and are very grateful to Dr Florian Menter and Dr Yuri Egorov of ANSYS for insightful discussions. Finally, this work is supported by the Vice-Chancellor PhD scholarship between Sheffield Hallam University and HORIBA MIRA Ltd.

Appendix A:

The pressure drag is calculated by obtaining the time-averaged pressure on the individual components from the numerical simulation. Using Equ. A1 and Equ. A2 the pressure drag is determined.

$$F_d = \iint p \; dydx \tag{A1}$$

$$C_d = \frac{2 * F_d}{\rho * {U_\infty}^2 * FA} \tag{A2}$$

Where *FA*, is the frontal area of the car considered without pins and ρ is the density of the air.

The pressure data obtained for all the angles investigated, and the MATLAB source code is supplied as a part of the supplementary material.

Appendix B:

Supplementary material – contains numerical predictions of pressure coefficient on the midplane, and pressure drag compared for SAE T20, T30, and T40 against the experiments. Velocity profiles and TKE on the backlight, boot deck and in the wake are compared amongst the angles investigated.

References:

Ahmed, S.R., Ramm, G., Faltin, G., 1984. Some Salient Features Of The Time-Averaged Ground Vehicle Wake, in: SAE International Congress and Exposition. SAE International. https://doi.org/https://doi.org/10.4271/840300

Aljure, D.E., Calafell, J., Baez, A., Oliva, A., 2018. Flow over a realistic car model: Wall modeled large eddy simulations assessment and unsteady effects. J. Wind Eng. Ind. Aerodyn. 174, 225–240. https://doi.org/10.1016/j.jweia.2017.12.027

Aljure, D.E., Lehmkuhl, O., Rodríguez, I., Oliva, A., 2014. Flow and turbulent structures around simplified car models. Comput. Fluids 96, 122–135. https://doi.org/10.1016/j.compfluid.2014.03.013

Ashton, N., Revell, A., 2015. Key factors in the use of DDES for the flow around a simplified car. Int. J. Heat Fluid Flow 54, 236–249. https://doi.org/10.1016/j.ijheatfluidflow.2015.06.002

Ashton, N., West, A., Lardeau, S., Revell, A., 2016. Assessment of RANS and DES methods for realistic automotive models. Comput. Fluids 128, 1–15. https://doi.org/10.1016/j.compfluid.2016.01.008

Carr, G.W., Stapleford, W.R., 1986. Blockage Effects in Automotive Wind-Tunnel Testing. https://doi.org/10.4271/860093

Cheng, S.Y., Tsubokura, M., Nakashima, T., Nouzawa, T., Okada, Y., 2011. A numerical analysis of transient flow past road vehicles subjected to pitching oscillation. J. Wind Eng. Ind. Aerodyn. 99, 511–522. https://doi.org/10.1016/j.jweia.2011.02.001

Cheng, S.Y., Tsubokura, M., Nakashima, T., Okada, Y., Nouzawa, T., 2012. Numerical quantification of aerodynamic damping on pitching of vehicle-inspired bluff body. J. Fluids Struct. 30, 188–204. https://doi.org/10.1016/j.jfluidstructs.2012.01.002

Cogotti, A., 1998. A Parametric Study on the Ground Effect of a Simplified Car Model, in: International Congress & Exposition. https://doi.org/10.4271/980031

Collin, C., Mack, S., Indinger, T., Mueller, J., 2016. A Numerical and Experimental Evaluation of Open Jet Wind Tunnel Interferences using the DrivAer Reference Model. SAE Int. J. Passeng. Cars - Mech. Syst. 9, 2016-01–1597. https://doi.org/10.4271/2016-01-1597

Evstafyeva, O., Morgans, A.S., Dalla Longa, L., 2017. Simulation and feedback control of the Ahmed body flow exhibiting symmetry breaking behaviour. J. Fluid Mech. 817, 817R21-817R212. https://doi.org/10.1017/jfm.2017.118

Fares, E., 2006. Unsteady flow simulation of the Ahmed reference body using a lattice Boltzmann approach. Comput. Fluids 35, 940–950. https://doi.org/10.1016/j.compfluid.2005.04.011

Forbes, D., Page, G., Passmore, M., Gaylard, A., 2017. A study of computational methods for

wake structure and base pressure prediction of a generic SUV model with fixed and rotating wheels. Proc. Inst. Mech. Eng. Part D J. Automob. Eng. 231, 1222–1238. https://doi.org/10.1177/0954407016685496

Fröhlich, J., Mellen, C.P., Rodi, W., Temmerman, L., Leschziner, M.A., 2005. Highly resolved large-eddy simulation of separated flow in a channel with streamwise periodic constrictions. J. Fluid Mech. 526, 19–66. https://doi.org/10.1017/S0022112004002812

Fröhlich, J., von Terzi, D., 2008. Hybrid LES/RANS methods for the simulation of turbulent flows. Prog. Aerosp. Sci. 44, 349–377. https://doi.org/10.1016/j.paerosci.2008.05.001

Grandemange, M., Cadot, O., Courbois, A., Herbert, V., Ricot, D., Ruiz, T., Vigneron, R., 2015. A study of wake effects on the drag of Ahmed's squareback model at the industrial scale. J. Wind Eng. Ind. Aerodyn. 145, 282–291. https://doi.org/10.1016/j.jweia.2015.03.004

Gritskevich, M.S., Garbaruk, A. V., Menter, F.R., 2013. Fine-tuning of DDES and IDDES formulations to the *k-ω* shear stress transport model. Prog. Flight Phys. 23–42. https://doi.org/10.1051/eucass/201305023

Gritskevich, M.S., Garbaruk, A. V., Schütze, J., Menter, F.R., 2012. Development of DDES and IDDES formulations for the k-ω shear stress transport model. Flow, Turbul. Combust. 88, 431–449. https://doi.org/10.1007/s10494-011-9378-4

Guilmineau, E., 2008. Computational study of flow around a simplified car body. J. Wind Eng. Ind. Aerodyn. 96, 1207–1217. https://doi.org/10.1016/j.jweia.2007.06.041

Guilmineau, E., Deng, G.B., Leroyer, A., Queutey, P., Visonneau, M., Wackers, J., 2018. Assessment of hybrid RANS-LES formulations for flow simulation around the Ahmed body. Comput. Fluids 176, 302–319. https://doi.org/10.1016/j.compfluid.2017.01.005

Guilmineau, E., Deng, G.B., Wackers, J., 2011. Numerical simulation with a DES approach for automotive flows. J. Fluids Struct. 27, 807–816. https://doi.org/10.1016/j.jfluidstructs.2011.03.010

Heft, A.I., Indinger, T., Adams, N.A., 2012. Introduction of a New Realistic Generic Car Model for Aerodynamic Investigations, in: SAE Technical Paper Series. https://doi.org/10.4271/2012-01-0168

Howard, R.J.A., Pourquie, M., 2002. Large eddy simulation of an Ahmed reference model. J. Turbul. 3, N12. https://doi.org/10.1088/1468-5248/3/1/012

Indinger, AIHT, Adams, N.A., 2012. Experimental and Numerical Investigation of Drivaer Model, in: Proceedings of the ASME 2012 Fluids Engineering Summer Meeting.

Islam, A., Thornber, B., 2017. High-order detached-eddy simulation of external aerodynamics over an SAE notchback model. Aeronaut. J. 121, 1342–1367. https://doi.org/10.1017/aer.2017.61

Islam, A., Thornber, B., 2016. Development and Application of a novel RANS and Implicit

les Hybrid Turbulence Model for Automotive Aerodynamics. SAE Tech. Pap. 2016-April. https://doi.org/10.4271/2016-01-1608

Keogh, J., Barber, T., Diasinos, S., Graham, D., 2016. The aerodynamic effects on a cornering Ahmed body. J. Wind Eng. Ind. Aerodyn. 154, 34–46. https://doi.org/10.1016/j.jweia.2016.04.002.

Khalighi, B., Zhang, S., Koromilas, C., Balkanyi, S.R., Bernal, L.P., Iaccarino, G., Moin, P., 2001. Experimental and Computational Study of Unsteady Wake Flow Behind a Bluff Body with a Drag Reduction Device, in: SAE International. pp. 1–15. https://doi.org/10.4271/2001-01-1042.

Krajnovic, S., Davidson, L., 2002. Large-eddy simulation of the flow around a bluff body. AIAA J. 40, 927–936. https://doi.org/10.2514/3.15142.

Krajnović, S., Davidson, L., 2005. Flow Around a Simplified Car, Part 1: Large Eddy Simulation. J. Fluids Eng. 127, 907. https://doi.org/10.1115/1.1989371.

Krajnović, S., Davidson, L., 2001. Large-Eddy Simulation of the Flow Around a GroundVehicle Body. SAE Tech. Pap. Ser. 2001. https://doi.org/10.4271/2001-01-0702

Le Good, G.M., Garry, K.P., 2004. On the Use of Reference Models in Automotive Aerodynamics. SAE Tech. Pap. 2004. https://doi.org/10.4271/2004-01-1308

Menter, F., 2018. Stress-Blended Eddy Simulation (SBES)—A New Paradigm in Hybrid RANS-LES Modeling, in: Notes on Numerical Fluid Mechanics and Multidisciplinary Design. pp. 27–37. https://doi.org/10.1007/978-3-319-70031-1_3

Menter, F., Kuntz, M., Bender, R., 2003. A Scale-Adaptive Simulation Model for Turbulent Flow Predictions. AIAA Pap. 2003–0767. https://doi.org/10.2514/6.2003-767

Menter, F.R., 2015. Best Practice: Scale-Resolving Simulations in ANSYS CFD, Ver. 2.00. ANSYS Inc 1–70. https://doi.org/10.1155/2013/859465

Menter, F.R., Kuntz, M., 2004. Adaptation of Eddy-Viscosity Turbulence Models to Unsteady Separated Flow Behind Vehicles, in: Lecture Notes in Applied and Computational Mechanics. pp. 339–352. https://doi.org/10.1007/978-3-540-44419-0_30

Mercker, E., 1986. A blockage correction for automotive testing in a wind tunnel with closed test section. J. Wind Eng. Ind. Aerodyn. 22, 149–167. https://doi.org/10.1016/0167-6105(86)90080-2

Onishi, K., Bale, R., Tsubokura, M., 2019. Assessment of rotating wheel vehicle aerodynamics simulation using cartesian grid method and open-grill full vehicle models. SAE Tech. Pap. 2019-April, 1–13. https://doi.org/10.4271/2019-01-0660

Piomelli, U., Chasnov, J.R., 1996. Large-Eddy Simulations: Theory and Applications BT -

Turbulence and Transition Modelling: Lecture Notes from the ERCOFTAC/IUTAM Summerschool held in Stockholm, 12–20 June, 1995, in: Hallbäck, M., Henningson, D.S., Johansson, A. V, Alfredsson, PH (Eds.), . Springer Netherlands, Dordrecht, pp. 269–336. https://doi.org/10.1007/978-94-015-8666-5_7

Pope, S.B., 2000. Turbulent Flows. Cambridge University Press, Cambridge. https://doi.org/DOI: 10.1017/CBO9780511840531

Read C., Viswanathan H., 2020. An Aerodynamic Assessment of Vehicle-Side Wall Interaction using Numerical Simulations. Int j. Automot. Mech. Eng. 17, 7587-7598. https://doi.org/10.15282/ijame.17.1.2020.08.0563.

Rezaeiha, A., Montazeri, H., Blocken, B., 2019. CFD analysis of dynamic stall on vertical axis wind turbines using Scale- Adaptive Simulation (SAS): Comparison against URANS and hybrid RANS /. Energy Convers. Manag. 196, 1282–1298. https://doi.org/10.1016/j.enconman.2019.06.081

Rodi, W., 1997. Comparison of LES and RANS calculations of the flow around bluff bodies.

J. Wind Eng. Ind. Aerodyn. 69–71, 55–75. https://doi.org/10.1016/S0167-6105(97)00147-5.

Serre, E., Minguez, M., Pasquetti, R., Guilmineau, E., Deng, G.B., Kornhaas, M., Schäfer, M., Fröhlich, J., Hinterberger, C., Rodi, W., 2013. On simulating the turbulent flow around the Ahmed body: A French-German collaborative evaluation of LES and DES. Comput. Fluids 78, 10–23. https://doi.org/10.1016/j.compfluid.2011.05.017

Shur, M.L., Spalart, P.R., Strelets, M.K., Travin, A.K., 2008. A hybrid RANS-LES approach with delayed-DES and wall-modelled LES capabilities. Int. J. Heat Fluid Flow 29, 1638–1649. https://doi.org/10.1016/j.ijheatfluidflow.2008.07.001

Spalart, P., Jou, W., Strelets, M., Allmaras, S., 1997. Comments of feasibility of LES for wings, and on a hybrid RANS/LES approach, in: International Conference on DNS/LES, Aug. 4-8, 1997, Ruston, Louisiana.

Wood, D., 2015. The Effect of Rear Geometry Changes on the Notchback Flow Field. PhD Thesis, Loughborough University. doi:https://hdl.handle.net/1234/18889.

Wood, D., Passmore, M.A., Perry, A.-K., 2014. Experimental Data for the Validation of Numerical Methods - SAE Reference Notchback Model. SAE Int. J. Passeng. Cars - Mech. Syst. 7, 2014-01–0590. https://doi.org/10.4271/2014-01-0590